Coupled hydrogen and fluorine incorporation in garnet: New constraints from FTIR, ERDA, SIMS, and EPMA

Jed L Mosenfelder, Anette von der Handt, Anthony C Withers, Hélène Bureau, Caroline Raepsaet, George R Rossman

Revision 1

Coupled hydrogen and fluorine incorporation in garnet: new constraints from FTIR, ERDA, SIMS, and EPMA

JED L. MOSENFELDER[1*], ANETTE VON DER HANDT[1], ANTHONY C. WITHERS[2], HÉLÈNE BUREAU[3], CAROLINE RAEPSAET[4], and GEORGE R. ROSSMAN[5]

[1] Department of Earth and Environmental Sciences, University of Minnesota, 116 Church St. SE, Minneapolis, Minnesota, 55455, U.S.A.

[2] Bayerisches Geoinstitut, Universität Bayreuth, 95440 Bayreuth, Germany.

[3] Institut de Minéralogie, de Physique des Matériaux et de Cosmochimie (IMPMC), Sorbonne Université, CNRS UMR 7590, Muséum National d'Histoire Naturelle, 4 place Jussieu, 75252 Paris Cedex 05, France.

[4] Service de Physique de l'état Condensé, SPEC, CEA, CNRS, Université Paris-Saclay, CEA Saclay, 91191 Gif sur Yvette, CEDEX, France.

[5] Division of Geological and Planetary Sciences, California Institute of Technology, M/C 170-25, Pasadena, California 91125-2500, U.S.A.

Word count: 13,992 (including abstract, references, and figure captions)

[*]E-mail: jmosenfe@umn.edu

ABSTRACT

It is well known that some garnet compositions can incorporate hydrogen and/or fluorine at levels up to several weight percent. However, accurate measurement of these elements can be difficult at trace to minor levels of abundance so they are frequently ignored in routine chemical analysis. Furthermore, the mechanisms of H incorporation are still under debate and only one mechanism for F substitution is commonly considered. We employed infrared spectroscopy (FTIR), elastic recoil detection analysis (ERDA), secondary ion mass spectrometry (SIMS), and electron probe microanalysis (EPMA) to measure H and F concentrations and constrain incorporation mechanisms in ten grossular garnets. We also present SIMS data for 11 spessartine and two andradite garnets. Three grossular garnets were measured with ERDA to obtain an infrared integral molar absorption coefficient (ε_i) for H_2O of 13,470 $L \cdot mol^{-1} \cdot cm^{-2}$. Grossular H_2O and F concentrations range from 0.017 to 0.133 wt% and 0.012 to 0.248 wt%, respectively. Correlations between ^{16}OH and ^{19}F and interpretation of FTIR spectra prompt us to consider various coupled substitutions of H and F for Si, which can explain some high frequency IR absorption bands that have been attributed previously to "hydrogrossular clusters" (variably-sized clusters in which 4H substitute for Si) or to inclusions of hydrous minerals. A strong correlation between ^{16}OH and ^{19}F in spessartine and similar high-frequency IR bands implies a similar role for H-F substitution. Coupled H-F substitution is also probably relevant to some andradite-rich garnets, rare pyrope from the Dora Maira massif, and some synthetic garnets. Improvements in analytical methods for trace to minor H and F open up more possibilities for using these elements to calculate the activities of H_2O and F-species in fluids that were in

equilibrium with garnet-bearing phase assemblages, as well as constraining the recycling of these elements into the mantle via study of xenoliths.

INTRODUCTION

Considerable progress has been made in the last three decades in understanding how trace amounts of hydrogen can be incorporated in nominally anhydrous minerals, and how this H (most commonly incorporated as structurally bound OH^- groups) affects geophysical and petrologic processes in the Earth and other planetary bodies. Recent work has also highlighted the potential importance of trace fluorine (substituting for O^{2-}) in nominally anhydrous minerals (Hervig and Bell 2005; Mosenfelder et al. 2011, 2015; Beyer et al. 2012; Bernini et al. 2012; Dalou et al. 2012; Mosenfelder and Rossman 2013a,b; Crépisson et al. 2014; Roberge et al. 2015; Grützner et al. 2017; Klemme and Stalder 2018; Yoshino and Vazhakuttiyakam 2018). In the case of garnets, a diverse supergroup of minerals widely distributed in the crust and mantle of the Earth, it has long been recognized that both H and F can be structurally incorporated at levels up to several weight percent (see Grew et al. 2013 for review). Researchers have taken advantage of this phenomenon to constrain the activities of H_2O and F-species in fluids in equilibrium with garnet-bearing phase assemblages (Manning and Bird 1990; Visser 1993; Arredondo et al. 2001; Chakhmouradian et al. 2008).

Hydrogen and/or F may in fact be almost ubiquitously present in trace to minor amounts in garnets, but are commonly ignored during chemical analysis because of difficulties inherent in measuring trace concentrations of light elements with commonly available techniques such as electron probe microanalysis (EPMA). Note that when we specify "H_2O" or "H" concentrations

in this paper we are primarily referring to the equivalent in structurally bound OH^- groups, because H is not incorporated in the form of structurally-bound H_2O groups in garnet.

Hydrogen can be detected easily using Fourier transform infrared spectroscopy (FTIR) in transmission mode, which also provides information on incorporation mechanisms, but uncertainties remain in absolute quantification using this method (Maldener et al. 2003; Rossman 2006). One of the best microanalytical techniques for trace F is secondary ion mass spectrometry (SIMS), which is highly sensitive owing to the ionization efficiency of both $^{19}F^-$ and $^{19}F^+$ and has benefited from technical advances that lower detection limits to less than 1 μg/g (Hauri et al. 2002; Koga et al. 2003; Mosenfelder et al. 2011). However, these measurements are most commonly made using F-bearing glasses for calibration, which can result in working curves with large uncertainties (Mosenfelder and Rossman 2013a).

SIMS measurements of H in garnets have primarily concentrated on pyrope-rich compositions representative of the mantle (Koga et al. 2003; Aubaud et al. 2007; Tenner et al. 2009), with one more recent study on grossular and spessartine (Reynes et al. 2018). Quantitative SIMS analyses of F in garnets are even more sparse (Jamtveit and Hervig 1994; Schingaro et al. 2016). In this study, we present new SIMS, FTIR, and EPMA data on the H and F concentrations of ten natural grossular garnets, and SIMS data on 11 spessartine and two andradite crystals. Furthermore, based on elastic recoil detection analysis (ERDA) of three grossular samples, we reassess calibrations for the IR molar absorption coefficient for H_2O derived by Rossman and Aines (1991) and Maldener et al. (2003). We demonstrate that H and F concentrations are strongly correlated in some garnets and suggest coupled H-F incorporation mechanisms analogous to those proposed for olivine by Crépisson et al. (2014). Coupled H-F substitution can rectify unexplained aspects of previous incorporation models for H in grossular, spessartine, and

pyrope (Aines and Rossman 1984; Rossman and Aines 1991; Cho and Rossman 1993; Reynes et al. 2018; Geiger and Rossman 2018, 2020a, 2020b).

ANALYTICAL METHODS

Sample selection and preparation

Table 1 lists the localities of the grossular garnets chosen for this study. Six of these garnets, derived from granulites of the Neoproterozoic Mozambqiue belt in Tanzania and Kenya (Giuliani et al. 2008, 2011), are referred to as "East African" in this paper. Additional details on the grossular, spessartine, and andradite samples used in the study are provided in the supplementary material.

Samples were prepared for analysis using previously described, epoxy-free polishing methods and cleaning procedures (Mosenfelder et al. 2011). The garnets were fabricated into doubly polished slabs that were first measured by FTIR and then sliced using a wire saw into multiple chips for analysis by different techniques; in all cases, individual chips originated from the same single crystal.

FTIR

Unpolarized infrared absorption spectra were collected for most of the garnets using the main compartment of either a Nicolet Magna 860 FTIR or Thermo-Nicolet iS50 FTIR at Caltech. All measurements employed a GLOBAR IR source, a KBr beamsplitter, and a MCT-A detector, with at least 512 scans taken at 2 cm^{-1} resolution. Analysis areas were selected using 200 to 400 μm diameter circular apertures and multiple spectra for each crystal were taken to assess the possibility of zoning. Sample thicknesses were measured using a Mitutoyo digital micrometer,

with a precision of ±2 μm. JLM83a was measured at UMN using a Hyperion 2000 microscope attached to a Bruker Tensor 37 spectrometer, with a GLOBAR IR source, a KBr beamsplitter, and a MCT-A detector. These spectra were collected on a slab ~390 μm thick, with 64 scans at 2 cm^{-1} resolution, using a 100 μm^2 square knife-edge aperture. The video-assisted mapping feature of the OPUS 7.2 software was employed to take regularly spaced data (in a 6 x 8 grid) across the central portion of the sample slab.

The low temperature (77 K) spectrum of GRR1386 was obtained in 1994 using a homebuilt vacuum chamber in the main compartment of the Nicolet 60SX FTIR that was operational at that time at Caltech. The room temperature spectrum of the sample taken in 1994 closely matches more recently acquired spectra.

Details of our baseline correction methods are provided in the supplementary material. After baseline correction, we calculated total integrated band areas in the O-H stretching region, referred to hereafter as Abs_{tot} (considered here as absorbance/cm^2 in one direction, rather than multiplying one measurement by three as in some studies on garnets). Spectra were then curve fitted using the Multipeak Fitting 2 package in Igor Pro software. Table 1 also gives values for the weighted mean wavenumber (as defined by Libowitzky and Rossman 1997) for each spectrum.

ERDA

In Table 2 we report hydrogen concentrations measured by ERDA for three grossular samples (GRR732, GRR771, and GRR1756), one synthetic forsterite (GRR1017), and three synthetic, rhyolitic glasses (NSL1, N3, and N5). The analyses were conducted at the Laboratoire d'Etudes des Eléments Légers, CEA, Saclay, France using improved methods for micro-ERDA

(Raepsaet et al. 2008, Bureau et al. 2009). Analytical methods followed those outlined by Withers et al. (2012) and are detailed in the supplementary material. GRR1017, well-characterized as an ultra-dry reference material with ≤0.007 μg/g H_2O (Mosenfelder et al. 2011), was used to assess the H background. Water contents of the rhyolitic glasses were previously reported in Tenner et al. (2009), measured using Karl-Fischer titration as described in Withers and Behrens (1999).

SIMS

SIMS data (Table 3) were obtained on the CAMECA 7f-GEO at Caltech using a Cs^+ primary ion beam and previously described methods optimized for collecting low-blank H and F analyses (Mosenfelder and Rossman 2013a; Mosenfelder et al. 2011, 2015). Data are presented from two sessions, conducted in 2012 and 2016. For each analysis, we acquired either 30 cycles (in 2012) or 20 cycles (in 2016) through the mass sequence ^{12}C, $^{16}O^1H$, ^{18}O, ^{19}F, and ^{30}Si, collecting negative ions with a mass resolution of ~5500 (ΔM/M), sufficient to separate $^{16}O^1H$ from ^{17}O and $^{18}O^1H$ from ^{19}F (Burdo and Morrison 1971). Analyses from 2012 were obtained from garnets pressed into the same indium mount as the orthopyroxenes, clinopyroxenes, olivines, and F-bearing glasses (MPI-DING glasses KL2-G and ML3B-G and USGS glasses BCR-2G and BHVO-2G) reported on previously (and analyzed during the same session) by Mosenfelder and Rossman (2013a,b). Some of the garnets were then extracted, re-polished, cleaned, and pressed together into a new indium mount with one additional garnet (JLM83a), the MPI-DING and USGS glasses, and five additional F-bearing glasses (Fba-1, 2, 3, 4 and 5) prepared by Guggino et al. (2011). We used the Fba-series glasses to reevaluate the F concentrations of our MPI-DING and USGS glass splits, as described in Mosenfelder et al.

(2020). The revised reference values used to establish working curves for F are given in the supplementary material.

$^{16}O^{1}H/^{18}O$ and $^{19}F/^{18}O$ ratios in Table 3 were blank corrected using $^{16}O^{1}H$ and ^{19}F backgrounds monitored by analyzing "blank" reference materials: synthetic forsterite GRR1017 (Mosenfelder et al. 2011), a natural Cr-rich pyrope from Ugelvik, Norway (GRR332), and laboratory-dehydrated grossular (GRR1122-HT) and spessartine (GRR2215-HT). Details on characterization of these samples are provided in the supplementary material.

EPMA

Electron microprobe analyses (Table 4) for most samples were acquired using a JEOL JXA-8900R at UMN. We first measured F, using MgF_2 as a standard; other elements were subsequently analyzed on the same spots using different analytical conditions. F kα was acquired on three TAP crystals simultaneously and intensities were then aggregated and combined with the other elements during post-processing with Probe for EPMA software (Probesoftware, Inc.). Despite its lower sensitivity for F Kα, we prefer TAP over LDE1 for this application, because LDE1 has the inherent problem of significant background interferences between the F Kα and Fe Kα, Mg Kβ, and Mn Kα X-ray lines (e.g., Witter and Kuehner 2004; Zhang et al. 2016). We found that an accelerating voltage of 20 kV optimized fluorescence yields and peak-to-background ratios for F on TAP. For most of the garnets, a beam current of 250 nA and beam diameter of 10 μm was used for this stage of the analysis. Analyses of JLM83a were conducted at either 200, 250, or 400 nA. Calculated detection limits range from ~40 at the highest current to 60 μg/g at the lowest current.

Using the procedure outlined by Donovan et al. (2011), an exponential background was fit to the F kα peak with parameters based on a detailed wavescan of Asbestos grossular. Counting times for each spectrometer were 400 seconds on peak and 350 seconds on each background position, resulting in aggregated times per analysis of 1200 seconds on peak and 2100 seconds on the background measurement. Time-dependent intensity (TDI) loss (or gain) was monitored for all elements, but no significant or systematic dependence was found so the TDI correction was not used. Unknown and standard intensities were corrected for deadtime and standard intensities were corrected for standard drift over time.

Major and minor elements were measured using an accelerating voltage of 15 kV, a beam current of 20 nA, and a beam diameter of 1 μm. Counting times for each element were 20 seconds on peak and 10 seconds at each background position. Reference materials used for calibration included synthetic forsterite (GRR1017) and tephroite (GRR392) for Mg and Mn, respectively; a natural almandine (Harvard 112140) for Fe; Asbestos grossular for Ca and Si; chromite (NMNH 117075) for Cr; ilmenite (NMNH 96189) for Ti; Brazilian spessartine (Verma, 1960) for Al; and vanadium metal for V. Na and K were also analyzed but were below the detection limit in all samples.

Final data processing used the CITZAF matrix correction method (Armstrong 1988), with FFAST mass absorption coefficients (Chantler et al. 2005). The matrix correction takes into account oxygen calculated by cation stoichiometry and the oxygen equivalent from F. Cation proportions (including reassignment of total Fe to Fe^{2+} and Fe^{3+}) and garnet end members were calculated using the Excel spreadsheet written by Locock (2008).

We also report EPMA data for two samples (GRR732 and GRR1429) that were acquired at Caltech using a JEOL JXA-8200. We used protocols for these analyses similar to those used at

UMN but did not measure F. Reference materials for calibration included synthetic pyrope for Mg, Al, and Si; synthetic tephroite (GRR392) for Mn; synthetic fayalite for Fe; grossular (GRR1386) for Ca; and synthetic rutile, Cr_2O_3, and V_2O_5 for Ti, Cr, and V, respectively.

RESULTS

FTIR spectroscopy

FTIR spectra representing the full variation in O-H stretching vibrations in the grossular samples we studied are displayed in Figure 1. Following Rossman and Aines (1991), these spectra can be separated into different classes according to the most prominent absorption bands present. Class 2, represented by GRR42 (Fig. 1a), is dominated by strong peaks at 3647, 3656, 3676, and 3687 cm^{-1}, with the highest peak at 3647 cm^{-1}. A subset of spectral class 2 is class 2b, which exhibits the same bands at high frequency (also with maximum absorbance at 3647 cm^{-1}) but has multiple bands between 3600 and 3500 cm^{-1} (Fig. 1a). Class 2b is represented by five of the East African garnets (GRR229, GRR732, GRR771, GRR1386a, and GRR1386), which have spectra with similar shapes but varying Abs_{tot} (Table 1 and supplemental Fig. S1). Three grossular garnets (GRR1122, GRR1429, and GRR1756) fall into class 7 in the Rossman and Aines scheme because their strongest absorption is at 3599 cm^{-1} rather than at 3647 cm^{-1}, but otherwise their spectra are similar to class 2b; class 2b and class 7 are compared on the same scale in Figure 1b.

The Asbestos garnet JLM83a (Fig. 1c) is typical of class 3, with a strong peak at 3631 cm^{-1} that is not as prominent in the other garnets. JLM83a also has bands centered at ~3621, 3644, 3659, 3665, 3677, and 3689 cm^{-1}. Garnets from Asbestos fall into both classes 3 and 4, where class 4 is defined by having its strongest peak at 3621 cm^{-1}. Figure 1c compares spectra of

JLM83a to published spectra of some other Asbestos grossular garnets (GRR53 and GRR1537) and end-member grossular crystals synthesized by Geiger and Armbruster (1997) and Withers et al. (1998).

Whereas the absorbance among different East African grossular varies widely (Table 1 and supplemental Fig. S1), we failed to detect H zoning within any individual single crystal from this area. The only crystals in our study that are significantly zoned, based on FTIR, are JLM83a and GRR1429. Abs_{tot} in JLM83a varied by a factor of ~2 in the range between 3750 and 3300 cm^{-1}. All spectra have similar shapes, but relative intensities of the peaks at 3631 and 3621 cm^{-1} vary (Fig. 1c). Rossman and Aines (1991) noted a comparable variation in Abs_{tot} for GRR53, from the same locality. Systematic zoning patterns (such as core-rim relationships or sector zoning) could not be deciphered in the randomly cut slab of JLM83a that we used for both FTIR and SIMS measurements. Although variations in absorbance in Asbestos garnets have been attributed previously to birefringence (Rossman and Aines 1986; Allen and Buseck 1988), our SIMS measurements (Table 3 and discussion below) demonstrate that actual differences in H concentration are a more important factor in this crystal.

GRR1429 is also birefringent, which might be the cause of the variations in Abs_{tot} (about 5% relative) in this sample. We used the average of seven baseline-corrected, unpolarized spectra taken on separate spots to estimate its H_2O content.

Close examination of the spectrum of GRR1386 (Fig. 1a) reveals 12 peaks between 3700 and 3500 cm^{-1} and the shoulders on some of the bands indicate that curve fitting should take into account more than 12 bands. Figure S5 in the supplementary material displays an example of curve fitting for this garnet. We fit 15 bands with a pseudo-Voigt profile (mixed Gaussian and Lorentzian), at 3531, 3539, 3546, 3567, 3583, 3599, 3608, 3623, 3631, 3643, 3647, 3657, 3664,

3674, and 3688 cm^{-1}. Although the fit is obviously non-unique, our peak positions (with initial guesses based on visual examination) are within 1 cm^{-1} of those fit for the same sample by Geiger and Rossman (2020a), with the slight difference that we fit an additional band at 3539 cm^{-1} not present in their fit. We used these peak positions as a basis to fit spectra for the other grossular garnets. Fitted peak centers in other samples are mostly within 1 cm^{-1} of those for GRR1386, with a few deviations up to 3 cm^{-1}. A table with the fit results for all samples is provided in the supplementary material.

The cooling experiment conducted on GRR1386 demonstrates that nearly all the mid-IR absorption in this garnet can be attributed to structurally incorporated O-H, with most bands shifting to higher energies upon cooling to 77 K (Fig. 2). There is no evidence for band splitting at low *T*, as observed in many other garnets (Geiger et al. 1991; Geiger and Rossman 2018). However, enlargement of the baseline region reveals a broad absorption band at ~3400 cm^{-1} that shifts to ~3240 cm^{-1}, typical of the transition from liquid water to ice (also plotted for comparison in Fig. 2 are spectra for water and ice from Bertie and Lan 1996 and Johnson and Rossman 2003). The 3400 cm^{-1} band is apparently also present in some of the other garnets, but quantification is hampered by high-frequency interference fringes in most spectra (not visible at the scales used in Fig. 1). The liquid water in GRR1386 is probably contained in sub-micrometer sized fluid inclusions, as found in other NAMs (e.g., Johnson and Rossman 2003; Mosenfelder et al. 2011). Its contribution to Abs_{tot} for this sample amounts to 1.2%. We have elected not to correct any of the estimates for Abs_{tot} in Table 1 for the possible presence of H_2O. Furthermore, we have ignored another possible contribution to Abs_{tot} in the O-H stretching region from the lowest energy spin-allowed Fe^{2+} transition in grossular with FeO content greater than 1 wt% (GRR42, GRR1122, GRR1386a, GRR1429, and JLM83a). This band should occur at lower

277 energy compared to other garnets (Geiger and Rossman 1994), because the larger size of the X
278 cation site in grossular leads to greater splitting of the Fe^{2+} bands (White and Moore 1972).
279 However, its exact position is difficult to determine owing to superposition of O-H stretching
280 vibrations (Slack and Chrenko 1971; White and Moore 1972).

281

282 **ERDA**

283 H_2O concentrations of the three grossular garnets, three rhyolitic glasses, and dry
284 forsterite as determined by ERDA are given in Table 2. ERDA and PIXE detector maps of the
285 analyzed areas for two of the garnets (GRR1756 and GRR732) revealed no significant
286 heterogeneities, but a small, anomalous region of interest with high H and Ca content in GRR771
287 was excluded in the calculation of its bulk H content. This "hot spot" probably represents surface
288 contamination (Withers et al. 2012). Bulk H (ERDA) and Ca (PIXE) maps for this sample are
289 provided in the supplementary material.

290 The nominal H_2O concentration measured by ERDA in GRR1017 forsterite, established
291 as an ultra-dry "blank" material with ≤ 0.007 μg/g H_2O (Mosenfelder et al. 2011), is 101±14
292 μg/g. The bulk H concentrations for grossular are strongly correlated with Abs_{tot} (Fig. 3). We
293 applied a York regression to the data (York et al. 2004; Vermeesch 2018), taking into account
294 uncertainties in both Abs_{tot} and the ERDA measurements. The regression yields an intercept of
295 100±13 μg/g H_2O, which is the value we subtract to arrive at the blank-corrected H_2O
296 concentrations. The slope of the fit line provides the following calibration for infrared
297 measurements:

298

299 $$C_{H_2O}\ (\mu g/g) = 0.370\ (\pm 0.035, 2\sigma) \times Abs_{tot} \quad (1)$$

This is the peer-reviewed, final accepted version for American Mineralogist, published by the Mineralogical Society of America.
The published version is subject to change. Cite as Authors (Year) Title. American Mineralogist, in press.
DOI: https://doi.org/10.2138/am-2021-7880. http://www.minsocam.org/

300

301 The integral molar absorption coefficient (ε_i, in L · mol^{-1} · cm^{-2}) can be derived by substituting
302 the above relation into a modified form of the Beer-Lambert law (e.g., Johnson and Rossman,
303 2004),

304

305 $$C_{H_2O}\ (\mu g/g) = Abs_{tot} \times 18.015 \times 10^6/[\rho \cdot \varepsilon_i], \quad (2)$$

306

307 where ρ is the density of the mineral (in g/L, or kg/m^3). Assuming for simplicity a typical density
308 for V-bearing grossular of 3615 kg/m^3 (Maldener et al. 2003), we derive a value for ε_i of 13,470
309 L · mol^{-1} · cm^{-2}.

310 A check on the accuracy of our ERDA data on grossular is provided by the results on the
311 three rhyolitic glasses, which are in excellent agreement with previously published total H_2O
312 concentrations determined for these samples using Karl-Fischer titration (Tenner et al. 2009).
313 The H_2O contents of the glasses measured by ERDA are within 5% of the reference values.

314

315 **SIMS and EPMA measurements of H and F**

316 SIMS data for the sessions conducted in 2012 and 2016 are summarized in Table 3, with
317 complete data for all individual analyses provided in the supplementary material. Statistics are
318 reported in this paper using the symbology of Fitzsimons et al. (2000). Internal precision in
319 $^{16}OH/^{18}O$ (calculated from $2s_{\bar{x}}$, the standard error of the mean for 20 or 30 cycles through the
320 mass sequence) ranged from 0.24 to 1.35% relative for all garnets except GRR1122-HT (the
321 blank) and JLM83a. Measured $^{19}F/^{18}O$ ratios were similarly precise (0.15 to 0.52%). The high

This is the peer-reviewed, final accepted version for American Mineralogist, published by the Mineralogical Society of America.
The published version is subject to change. Cite as Authors (Year) Title. American Mineralogist, in press.
DOI: https://doi.org/10.2138/am-2021-7880. http://www.minsocam.org/

variability in internal precision as well as external precision (reproducibility) for JLM83a is discussed below.

$^{16}OH/^{18}O$ for each garnet with the exception of JLM83a is plotted in Figure 4 as a function of H_2O concentration determined from FTIR data using the ERDA calibration. Similar plots are derived if ^{30}Si is used instead of ^{18}O as the reference mass. Uncertainties in H_2O concentration were estimated by propagating the error in Abs_{tot} (Table 1) and the uncertainty in the fit to the ERDA data (Fig. 3 and Equation 1). York regressions applied to the data for East African garnets (GRR229, GRR732, GRR771, GRR1386, GRR1386a, and/or GRR1756) have indistinguishable slopes for the two sessions. These regressions also fit well to the data for GRR1429 and GRR1122 measured in 2012. However, the 2016 data for GRR1122 are significantly offset from the regression line, as are both the 2012 and 2016 data for GRR42.

In the case of GRR1122 we provisionally attribute this discrepancy to heterogeneity in the sample not recognized from FTIR data and insufficiently probed by the six SIMS analyses that were acquired. The heterogeneity could be related to the presence of fluid inclusions, indicated by a weak broad band at 3420 cm^{-1} similar to that seen in GRR1386 (Fig. 2). As for GRR42, the consistency in values for seven analyses from the two sessions suggests a different explanation for the offset from the regression. In the discussion section, we explore the possibility that the H concentration of GRR42 is significantly underestimated owing to the frequency dependence of the IR molar absorption coefficient, which cannot be accurately constrained from our ERDA data.

Fluorine concentrations measured by SIMS and EPMA are compared in supplemental Figure S8. The SIMS concentration values are tied to our redetermination of reference values for the F-bearing basaltic glasses we regularly use for calibration, not taking into account any

345 possible SIMS matrix effect. The close correspondence between SIMS and EPMA values (with
346 all values reasonably close to the 1:1 line) suggests that any such matrix effect is minimal in this
347 case.

348 The heterogeneity in apparent H_2O concentrations measured by FTIR in JLM83a was
349 confirmed by the grid map of SIMS analyses taken over approximately the same area (Fig. 5).
350 The SIMS analyses also reveal heterogeneity in F, which was additionally confirmed by EPMA
351 (see supplementary material). The measurements using SIMS, FTIR, and EPMA cannot be
352 compared directly to determine a zoning pattern because the FTIR analyses are taken in
353 transmission, whereas the SIMS and EPMA measurements sample a volume that is close to the
354 surface (~1-2 μm deep for SIMS, and ~3 μm deep for EPMA at the analytical conditions used).
355 However, the range in apparent H_2O concentrations measured by FTIR (256-571 μg/g) is similar
356 to the range measured by SIMS (170-576 μg/g), calculated by applying the York regression in
357 Figure 4b. For the sake of this comparison we discard four analyses (marked by asterisks in Fig.
358 5) that were affected by the spike in background contaminant levels in the vacuum caused by the
359 cold trap running out of liquid N_2 (see supplementary material). These analyses had $^{12}C/^{18}O$
360 ratios one to two orders of magnitude higher than the other analyses.

361 Following the 2012 session, it became apparent that ^{19}F and ^{16}OH are correlated for
362 some grossular garnets, particularly the East African samples with similar class 2b and class 7
363 FTIR spectra (Fig. 6a). A similar correlation was noted for spessartine (Fig. 6b). An even more
364 robust correlation exists for the data taken on JLM83a alone (Fig. 6a). The values in Figure 6a
365 for JLM83a represent average $^{16}OH/^{18}O$ and $^{19}F/^{18}O$ for each analysis. However, the internal
366 precision of the analyses varies widely, with $s_{\bar{x}}/\hat{s}_{\bar{x}}$ (where $\hat{s}_{\bar{x}}$ is the precision predicted by
367 Poisson statistics; Fitzsimons et al., 2000), ranging from 1 (ideal) to 30 (poor). We would

normally discriminate against SIMS measurements with such high $s_{\bar{x}}/\hat{s}_{\bar{x}}$ values; for instance, in Mosenfelder et al. (2011) all analyses of olivine with $s_{\bar{x}}/\hat{s}_{\bar{x}} > 5$ were filtered out. High $s_{\bar{x}}/\hat{s}_{\bar{x}}$ in olivine and orthopyroxene has been attributed to the presence of sub-micrometer to micrometer-sized inclusions of hydrous minerals (such as serpentine and amphibole) and/or fluid inclusions (Mosenfelder et al. 2011; Mosenfelder and Rossman 2013a). In the present case, however, we attribute the high variability to zoning in H and F within the garnet itself. Analyses with high $s_{\bar{x}}/\hat{s}_{\bar{x}}$ show strong cycle-to-cycle covariation between ^{19}F and ^{16}OH (Supplementary Fig. S8), indicating that F and H are coupled on a sub-micrometer scale.

DISCUSSION

Molar IR absorption coefficient for H_2O in grossular

In Figure 7, we compare our ERDA data to H_2O concentrations measured (as a function of Abs_{tot}) in grossular-rich garnets using other "absolute" techniques: NRA (Rossman and Aines 1991; Maldener et al. 2003), P_2O_5 cell coulometry using a moisture evolution analyzer (MEA, Aines and Rossman 1984), H manometry (Aines and Rossman 1984), and continuous-flow mass spectrometry (O'Leary et al., 2007). Also displayed in the graph is the regression line for all of the data considered by Rossman and Aines (1991) for grossular and hydrogrossular with up to 12.75 wt% H_2O (with H_2O contents on the high end well-constrained using X-ray diffraction).

We have no definitive explanation for the discrepancy between H concentrations measured in GRR732 by ERDA (599 μg/g H_2O) and continuous-flow mass spectrometry (CFMS; 1062 μg/g H_2O); we can only speculate that the blank for that particular CFMS measurement was higher than recognized. Our data show excellent agreement, however, with some of the NRA data. In particular, the analyses by Maldener et al. (2003) on their TSAV (480

This is the peer-reviewed, final accepted version for American Mineralogist, published by the Mineralogical Society of America.
The published version is subject to change. Cite as Authors (Year) Title. American Mineralogist, in press.
DOI: https://doi.org/10.2138/am-2021-7880. http://www.minsocam.org/

391 ± 40 μg/g H_2O) and thin (0.0165 cm) slab of HESS1 (870 ± 90 μg/g H_2O) samples lie close to
392 our regression line. These East African grossular garnets have IR spectra similar to those from
393 the same area that we measured with ERDA. Our data are in poorer agreement with Maldener et
394 al.'s analyses of a thicker (0.0312 cm) slab of HESS1 (950 ± 80 μg/g H_2O) and with MALI (170
395 ± 20 μg/g H_2O) and GRMALI (190 ± 20 μg/g H_2O). The two NRA measurements of HESS1 are
396 in agreement with each other within mutual uncertainties, which suggests that there is a
397 discrepancy in the FTIR measurements (e.g., non-linearity of the detector for linear absorbance
398 higher than 1.5 in the thick HESS1 sample) or perhaps unrecognized H zoning in the crystal. The
399 discrepancies between our measurements and those on MALI and GRMALI might derive from
400 errors made in correcting the sample thicknesses for beam convergence in the microscope.
401 Furthermore, any inaccuracies in blank correction are also more likely to affect these low H
402 content samples.
403 The H concentrations of Asbestos grossular garnets GRR53 and GRR53F were measured
404 using three different techniques: H manometry, MEA, and NRA (Aines and Rossman 1984;
405 Rossman and Aines 1991). The poor agreement of our data fit with the values determined with
406 those techniques might be related to H zoning comparable to that in JLM83a. Hydrogen
407 manometry and MEA are bulk methods that sample a much larger volume than the FTIR
408 measurements and thus cannot account for fine-scale zoning. Even though NRA is a near-surface
409 technique, the beam size employed at that time was much larger (several mm) than the apparent
410 scale of H zoning in Asbestos grossular. Furthermore, the NRA measurement of GRR53F
411 employed a reaction with ^{19}F ions that was subsequently abandoned in favor of a more
412 reproducible reaction employing a ^{15}N beam (Rossman 2006).

This is the peer-reviewed, final accepted version for American Mineralogist, published by the Mineralogical Society of America.
The published version is subject to change. Cite as Authors (Year) Title. American Mineralogist, in press.
DOI: https://doi.org/10.2138/am-2021-7880. http://www.minsocam.org/

There is a large discrepancy (Fig. 7) between our data fit on relatively low H content grossular and the regression applied by Rossman and Aines (1991), which was largely constrained by hydrogrossular garnets with high H contents. The discrepancy cannot be attributed to the lower sample density of hydrogrossular; for instance, using Equation 2, Crestmore hydrogrossular GRR1358, which has 12.75 wt% H_2O, Abs_{tot} of 158,750 cm^{-2}, and a calculated density of 3050 kg/m^3 (Basso et al. 1983), would have an ε_i of 7354 $L \cdot mol^{-1} \cdot cm^{-2}$, lower than our new value by a factor of almost two. The data on hydrogrossular samples could have been compromised by uncertainties in sample thickness or unrecognized H zoning, but these factors are speculative and more work is needed to ascertain the reason for the large apparent difference between low-H grossular and hydrogrossular.

The possibility of a difference in calibration factor for grossular and hydrogrossular was already noted by Rossman and Aines (1991), and Rossman (2006) recommended a calibration factor for low H content grossular of 0.14 (for absorbance in three directions). That value, equivalent to 0.42 for the convention for Abs_{tot} used in this study, compares reasonably well to our new value of 0.370 ±0.035 (Equation 1). We conclude that our new calibration is more appropriate than the Rossman and Aines calibration for grossular with less than ~1 wt% H_2O.

Empirical and theoretical studies consistently show an increase in ε_i with decreasing frequency for O-H absorption bands (Paterson 1982; Libowitzky and Rossman 1997; Balan et al. 2008; Mosenfelder et al., 2015). This means that an IR calibration based on grossular with relatively low mean wavenumber might underestimate the H_2O contents of grossular with higher mean wavenumber. Whereas our ERDA calibration was performed on grossular with mean wavenumbers between 3595 and 3622 cm^{-1} (Table 1), GRR42 is dominated by bands with significantly higher frequency (with a mean wavenumber of 3647 cm^{-1}; Fig. 1a, Table 1). A

436 frequency dependence to ε_i can therefore explain the offset of SIMS data for this sample in
437 Figure 4, but the magnitude of the dependence is poorly constrained. For the sake of calculating
438 formula units and garnet end-members (Table 4), we assume a H_2O concentration for this sample
439 based on the York regression shown in Figure 4a. Further work is needed to constrain the
440 frequency dependence of ε_i to determine whether this assumption is justified. Our calibration
441 also might underestimate H_2O concentrations for JLM83a and other Asbestos grossular garnets,
442 which also have a higher mean wavenumber (Table 1). Unfortunately, the zoning in some (or
443 all?) of these class 3 and 4 garnets will make this goal challenging, and class 2 garnets with
444 spectra like that of GRR42 are rare in our experience. A better way forward might entail
445 synthesizing grossular crystals at high *P-T* (Geiger and Armbruster 1997; Withers et al. 1998)
446 and establishing their homogeneity using a technique such as ERDA.
447
448 **Previous models of H and F incorporation mechanisms**
449 Hydrogen incorporation in garnets is classically assumed to take place via the
450 "hydrogarnet" substitution, whereby four H atoms bond to the O atoms surrounding a vacant Si
451 site. Hereafter, we refer to this substitution as $(4H)_{Si}^{\times}$, which is a commonly used, abbreviated
452 form of the following defect associate written in Kröger-Vink (1956) notation:
453
454 $$\left\{V_{Si}^{''''} - 4(OH)_O^{\cdot}\right\}^{\times}. \quad (3)$$
455
456 Here, *V* represents a vacancy; the superscripts $^{\times}$, $^{\cdot}$ and $'$ represent null, positive, and negative
457 charges relative to the perfect structure, respectively; and the subscripts refer to Si and O
458 crystallographic sites. We recognize that some mineralogists might object to using point defect

This is the peer-reviewed, final accepted version for American Mineralogist, published by the Mineralogical Society of America.
The published version is subject to change. Cite as Authors (Year) Title. American Mineralogist, in press.
DOI: https://doi.org/10.2138/am-2021-7880. http://www.minsocam.org/

459 symbolism to refer to both trace and high concentrations of elements, but we use it in the
460 following discussion for the sake of convenience.

461 The $(4H)_{Si}^{\times}$ mechanism is well established for H-rich garnets along the grossular-katoite
462 join (for review, see Beran and Libowitzky 2006; Grew et al. 2013; and Geiger and Rossman
463 2020a), not only from chemistry but from NMR, X-ray diffraction (XRD), and neutron
464 diffraction (Cohen-Addad et al. 1987; Lager et al. 1987, 1989; Cho et al. 1993). An analogous
465 substitution of four F atoms substituting for O surrounding a vacant Si site is well documented
466 for F-rich garnets, based on XRD (Smyth et al. 1990; Chakhmouradian et al. 2008) and negative
467 correlations between Si and F concentrations (Flohr and Ross 1989; Visser 1993;
468 Chakmouradian et al. 2008). This substitution can be written as:

469

470 $$\left\{V_{Si}^{''''} - 4(F)_O^{\cdot}\right\}^{\times}. \quad (4)$$

471

472 This substitution differs structurally from $(4H)_{Si}^{\times}$ in the sense that F atoms can occupy the
473 regular site of O atoms, whereas the H atoms in $(4H)_{Si}^{\times}$ are bonded to O that is displaced from its
474 normal position owing to expansion of the tetrahedron (e.g. Lager et al. 1989).

475 Other substitution mechanisms for H and particularly for F in garnet have received
476 somewhat less attention. Valley et al. (1983) considered the possibility, in addition to
477 mechanisms (3) and (4), of F and H incorporation in grossular via the coupled substitution:

478

479 $$(Al, Fe)^{3+} + O^{2-} \leftrightarrow (Mg, Fe)^{2+} + (F, OH)^{-}, \quad (5)$$

480

where the cations are located in the six-coordinated Y site. They recognized that verification of this substitution relies on accurate determination of Fe^{2+}/Fe^{3+} as well as H and F content, beyond the scope of their study. Various mechanisms involving coupled substitution of Ti and H have also been considered, primarily for pyrope (Bell and Rossman 1992; Khomenko et al. 1994; Geiger et al. 2000) but also for grossular (Reynes et al. 2020). Partial substitution of H for the Y-cation in a hydrogrossular was inferred by Kalinichenko et al. (1987), based on NMR, and at least two studies have inferred substitutions other than $(4H)^{\times}_{Si}$ in H-rich garnets based on crystal chemical arguments (Birkett and Trcienski 1984; Basso and Cabella 1990). In principle OH^- or F^- can replace O in the dodecahedral X-site in garnet, if it is vacant or contains a monovalent cation (e.g., Andrut et al. 2002). For instance, a Ca vacancy in grossular can be compensated by two H, which we notate as $(2H)^{\times}_{Ca}$. A similar substitution for the Y cation can be notated as $(3H)^{\times}_{Al}$ or $(3H)^{\times}_{Fe}$, depending on the garnet composition.

Early on in the study of nominally anhydrous minerals it was recognized that the mid-IR spectra of some garnets are incompatible with the $(4H)^{\times}_{Si}$ mechanism, because too many peaks are present (Aines and Rossman 1984). The $(4H)^{\times}_{Si}$ substitution *sensu stricto* (cf. Geiger and Rossman 2020a; see below) can result in a maximum of four O-H stretching vibrations, or two if the symmetry of the garnet is maintained (Harmon et al. 1982; Aines and Rossman 1984). The IR spectra of many pyrope, almandine, and andradite garnets are dominated by a broad, asymmetric band that splits into two bands at low temperature (cooled by liquid N_2), thus consistent with $(4H)^{\times}_{Si}$ (Geiger et al. 1991; Geiger and Rossman 2018). Differences in band positions as a function of composition can be explained by the presence of different neighboring X and Y cations, and the broad width of the bands can be explained by a combination of proton disorder and variations in local cation configuration. On this basis, Geiger and Rossman (2018)

assigned bands at 3629, 3613, 3598, and 3563 cm^{-1} in pyrope, almandine, grossular, and andradite respectively to $(4H)^{\times}_{Si}$. However, in grossular, as well as many spessartine garnets (Aines and Rossman 1984; Arredondo et al. 2001) and some rare pyrope garnets from the Dora Maira massif (Rossman et al. 1989), the multitude of sharp peaks cannot be explained by this mechanism alone.

Additional constraints on H incorporation in grossular and garnets on the grossular-andradite join come from experimental studies of H diffusion (Kurka et al. 2005; Phichaikamjornwut et al. 2012; Reynes et al. 2018). All of these studies support the idea that there are multiple sites for O-H incorporation, because various O-H bands decrease at different rates during dehydration. In general, dehydration kinetics for bands at higher frequency have a lower activation energy (E_a) than those at low frequency. For instance, Reynes et al. (2018) measured E_a for a grossular-rich garnet in the range between 157 and 185 $kJmol^{-1}$ for bands at 3628, 3645, 3657, and 3686 cm^{-1}, and in the range between 216 and 275 $kJmol^{-1}$ for bands at 3533, 3576, and 3604 cm^{-1}. A positive dependence of the diffusion coefficient on f_{O_2} as well as observations of color changes in sample rims in the experiments by Reynes et al. also support a key role for Fe^{2+} in dehydration. Reynes et al. identify a fast diffusion mechanism, analogous to that identified in many other nominally anhydrous minerals (Ingrin and Blanchard 2006), that is limited by the availability of Fe^{2+}:

$$M^{2+} + OH^{-} + \frac{1}{4}O_2 \rightarrow M^{3+} + O^{2-} + \frac{1}{2}H_2O, \quad (6)$$

where M represents either Fe or Mn, which may or may not be directly tied to a defect responsible for incorporating H. Our failed attempt to fully dehydrate GRR1122 (supplementary

Fig. S4) at low f_{O_2} (with virtually no change in spectra between dehydration steps 1 and 2) is consistent with this interpretation. We will return to this point when we discuss our model for coupled H-F substitution in the next section.

Another critical constraint on H incorporation in grossular comes from the study of Cho and Rossman (1993), who performed solid-state ^{1}H NMR measurements on a synthetic end-member katoite ($Ca_3Al_2\square_3(OH)_{12}$) powder and single crystals of GRR1386 (Fig. 1a), GRR53 (Fig. 1c), and GRR1537 (Fig. 1c). From their analysis of multiple-quantum spectra, Cho and Rossman concluded that the protons in katoite occur in closely spaced groups of four, as expected for $(4H)^{\times}_{Si}$. However, the best fit to the multi-quantum spectrum of GRR1386 was for a cluster size of two protons, and the best fit to the data for GRR1537 was for two separate clusters consisting of two and four protons each. The class 4 IR spectrum of GRR1537 is dominated by a band at 3621 cm^{-1} (Fig. 1c), which is the position of the main band in a synthetic hydrogrossular with composition $Ca_3Al_2(SiO_4)_{2.28}(O_4H_4)_{0.72}$ (Rossman and Aines 1991). Therefore, Cho and Rossman assigned this band to $(4H)^{\times}_{Si}$ and other, less intense bands to a different, unspecified defect containing two closely spaced protons.

Geiger and Rossman (2020a, 2020b) offered a novel explanation for the sharp, high-frequency bands in natural grossular. They hypothesized that bands at 3599, 3612, 3622, 3634, and 3641 cm^{-1} correspond to clustered groups of $(4H)^{\times}_{Si}$ with cluster sizes of one, two, three, four and five, respectively. A band at 3657 cm^{-1} was tentatively assigned to a cluster size of six, and a band at 3660 cm^{-1} was assigned to a "finite size katoite cluster" based on the fact that the main absorption in pure katoite (GRR1059; mislabeled as "Si 2.28" in Fig. 7 of Geiger and Rossman 2020a) occurs at this frequency (Rossman and Aines 1991). Bands at 3674 and 3688 cm^{-1} were

549 attributed to inclusions of hydrous minerals. This model explains all the features in IR spectra of
550 class 2, 3, and 4 grossular and all absorptions above ~3600 cm^{-1} in class 2b.

551 It is well known from studies of hydrous minerals that the strengths of O-H bonds (and
552 thus their vibrational frequencies) are affected by different cations sharing bonds with the same
553 O atom (i.e., second nearest neighbors to the H atom). For example, the frequencies of O-H
554 bonds in amphibole, which vary by up to ~50 cm^{-1}, can be reliably assigned to different cation
555 environments (e.g., Burns and Strens 1966). Recent work has also explored the effects of
556 neighboring cations on O-H stretching frequencies in olivine (Blanchard et al. 2017). The cluster
557 model of Geiger and Rossman (2020a,b), however, relies on an assumption that comparable
558 shifts in O-H bond frequencies are influenced by bonds in other $(4H)^{\times}_{Si}$ that are not directly
559 adjacent, because the tetrahedra in garnet are isolated from each other. Geiger and Rossman
560 justify this assumption as a consequence of the increase in Ca-O bond lengths between the end
561 members grossular (Geiger and Armbruster 1997) and katoite (Lager et al. 1987). It remains to
562 be shown by first-principles modeling or other methods whether or not this relaxation in Ca-O
563 distances for the end members also operates on a localized scale within small, isolated clusters of
564 $(4H)^{\times}_{Si}$ in garnets with trace amounts of H. It should also be noted that the model of Geiger and
565 Rossman ignores the results of Cho and Rossman (1993) that indicate some grossular garnets
566 contain a significant fraction of defects with only two protons. Furthermore, the assignment of
567 bands at 3674 and 3688 cm^{-1} to inclusions of hydrous phases is problematic, owing to geological
568 and spectroscopic reasons that we elaborate in the supplementary material. In the following
569 sections, we offer alternative explanations for some of the absorption bands that call on coupled
570 H and F substitution for Si as well as substitution of H (and possibly F) for cations in octahedral
571 and/or dodecahedral sites.

572

573 **Coupled substitution of H and F**

574 Our first clue that incorporation mechanisms of H and F in grossular might be entangled
575 came from correlations between ^{16}OH and ^{19}F in grossular (Fig. 6a) and spessartine (Fig. 6b),
576 prompting us to consider coupled substitution of H and F for Si (or other cations). While it is
577 possible that these correlations are coincidental and reflect nothing about coupled H-F
578 substitution, interpretation of the IR spectra combined with quantitative data on H and F
579 concentrations (Table 4) suggests otherwise.

580 Consider first the comparison between GRR42 and GRR1386: these crystals have the
581 same F content (0.25 wt%), but GRR1386 has nearly twice as much H_2O (0.13 wt%) as GRR42
582 (0.07 wt%; based on SIMS). The other obvious difference (Fig. 1a) is that both garnets have
583 significant absorbance above ~3620 cm^{-1}, but GRR42 has much lower absorbance at lower
584 frequencies. This suggests that some of the high-frequency bands are related to defects
585 containing both H and F, unless all F is bound in anhydrous defects (e.g., via Equation 4). We
586 draw a similar conclusion from the comparison between GRR732 and GRR1122 in Figure 1b:
587 these garnets have nearly the same H_2O content (0.052-0.054 wt%), but GRR732 has almost
588 twice as much F (0.11 wt%) as GRR1122 (0.06 wt%) and has stronger absorbance above ~3620
589 cm^{-1}, whereas GRR1122 has stronger absorbance at lower frequencies. Furthermore, the
590 strongest correlation between ^{16}OH and ^{19}F is evident in JLM83a, which has virtually no
591 absorbance at frequencies lower than ~3600 cm^{-1} (Fig. 1c) – again suggesting that the higher-
592 frequency O-H bands are related to F incorporation. An attempt to quantify these general
593 observations is summarized in Figure 8, where we plot F (per formula unit, Table 4) against the
594 band areas derived by spectral curve fitting for nine out of ten of the grossular garnets in the

595 study (JLM83a is excluded from this analysis because it is difficult to compare any given
596 spectrum to a precise F content in this zoned garnet).

597 Motivated partly by these observations and partly by the experiments and first-principles
598 density functional theory (DFT) calculations of Crépisson et al. (2014) on forsterite, we propose
599 that some of the bands at frequencies > 3600 cm^{-1} represent coupled H-F substitution for Si.
600 Following Cho and Rossman (1993) and Withers et al. (1998), we start with the assumption that
601 the band at 3621 cm^{-1}, with a shoulder at ~3610 cm^{-1}, represents $(4H)_{Si}^{\times}$. The asymmetry of the
602 stretching vibration in this region is consistent with the band structure in other garnet
603 compositions previously assigned to $(4H)_{Si}^{\times}$ (Geiger and Rossman 2018), although the bands in
604 grossular are narrower. Some or all of the bands at higher frequencies are then assigned to defect
605 associates involving both OH^- and F^-:
606
607 $$\left\{V_{Si}^{''''} - (OH)_O^{\cdot} - 3(F)_O^{\cdot}\right\}^{\times} \quad (7)$$
608 $$\left\{V_{Si}^{''''} - 2(OH)_O^{\cdot} - 2(F)_O^{\cdot}\right\}^{\times} \quad (8)$$
609 $$\left\{V_{Si}^{''''} - 3(OH)_O^{\cdot} - (F)_O^{\cdot}\right\}^{\times} \quad (9)$$
610
611 Calculations made by Crépisson et al. (2014) indicate that some of these clumped OH-F
612 defects in forsterite lead to O-H vibrations at higher frequencies than those assigned by previous
613 studies to the $(4H)_{Si}^{\times}$ defect. For instance, the single O-H stretching vibration corresponding to
614 defect (7) is at 3674 cm^{-1}, as opposed to the four O-H vibrations predicted for the most stable
615 $(4H)_{Si}^{\times}$ configurations, which are between ~3400 and 3625 cm^{-1} (Balan et al. 2011; Umemoto et
616 al. 2011). In general, the frequencies of bands assigned to the various clumped OH-F defects
617 decrease as the number of F atoms decreases, but complexities arise owing to the three non-

This is the peer-reviewed, final accepted version for American Mineralogist, published by the Mineralogical Society of America.
The published version is subject to change. Cite as Authors (Year) Title. American Mineralogist, in press.
DOI: https://doi.org/10.2138/am-2021-7880. http://www.minsocam.org/

equivalent crystallographic sites for O in the olivine structure. A positive frequency shift is also predicted for a clumped OH-F defect in an octahedral site, compared to a fully protonated vacancy. The positive O-H frequency shifts for sites where F^- replaces O^{2-} are presumably a consequence of the influence of F^- (which is more electronegative than O^{2-}) on the geometry of the polyhedron (Crépisson et al. 2014). The theoretically derived frequencies of the clumped OH-F defects represented by Equations 7-9 are consistent with IR spectra of natural olivines known to contain relatively high F concentrations (Sykes et al. 1994; Libowitzky and Beran 1995; Mosenfelder et al. 2011), which have bands at 3670, 3637, and 3620 cm^{-1} that are not present in olivines with lower F contents.

Precise assignment of individual high-frequency bands in grossular to defects represented by Equations 7-9 is difficult. We tentatively assign the band at 3687-3688 cm^{-1} to Equation (7), by analogy to the corresponding defect in olivine. This attribution helps to reconcile the H diffusion behavior observed by Kurka et al. (2005), who found that this band and the band at 3600 cm^{-1} decrease more rapidly than bands at 3645 and 3568 cm^{-1}. Specifically, H diffusion of the defect associated with Equation 7 can take place rapidly via the reaction:

$$\left\{V''''_{Si} - (OH)^{\cdot}_{O} - 3(F)^{\cdot}_{O}\right\}^{\times} + Fe^{\times}_{Ca} + \frac{1}{4}O_2 = \left\{V''''_{Si} - (O)^{\times}_{O} - 3(F)^{\cdot}_{O}\right\}^{'} + Fe^{\cdot}_{Ca} + \frac{1}{2}H_2O. \quad (10)$$

This reaction is similar to the generalized redox reaction represented by Equation (6) but is defect-specific. In this case, F diffusion – which is inherently slower than H diffusion – is not needed to maintain charge balance because dehydration involves oxidation of Fe^{2+} in the dodecahedral site. Many studies have found that oxidation reactions of this type are faster than reactions that require counter-diffusion of cations to maintain charge balance (Ingrin and

Blanchard 2006), and Reynes et al. (2018) provide direct evidence from color changes in dehydrated crystals and experiments at variable f_{O_2} that oxidation of Fe^{2+} plays a key role in dehydration of grossular.

The effect of dilute F substitution on local symmetry of the grossular structure is unknown, so it is not straightforward to use group theory to predict how many bands should be present for defects containing more than one O-H bond (Equations 8 and 9). Significant proportions of cations other than Ca and Al in neighboring X and Y sites, such as V or Fe (present in some of the grossular garnets in this study; Table 4), could also shift the frequencies of the O-H bands, because these frequencies largely depend on the masses, ionic radii, and electronic states of the neighboring cations (Burns and Strens 1966; Berry et al. 2007; Geiger and Rossman 2018, 2020a). This effect is likely to be minor but may explain the small shifts up to 3 cm^{-1} for some peaks in our curve fits for different grossular spectra. The imperfect correlation of F to the integrated absorbance of the high-frequency bands (Fig. 8a) could be related to the additional presence of F in sites with no OH (e.g., Equation 4), vagaries of the fitting exercise, or perhaps other mechanisms completely unrelated to F – such as the cluster model of Geiger and Rossman (2020a,b) or coupled substitution of H and Ti (Reynes et al. 2020), which we discuss below. Therefore, more work including ab initio calculations is needed to verify our hypothesis that clumped OH-F defects are present in grossular. One attractive feature of our model is that the presence of a significant proportion of defect (8) could partially explain the finding of Cho and Rossman (1993) that H is predominantly present in clusters of two closely spaced protons in GRR1386, and by extension to other class 2b grossular garnets.

Low frequency O-H absorption bands

No study has yet offered a satisfactory explanation for all the bands below ~3600 cm^{-1} in class 2a and class 7 grossular (some of the bands are also present in class 5 and 6 grossular; Rossman and Aines 1991). Geiger and Rossman (2020a) assigned the band at 3563 cm^{-1} to a localized "hydroandradite group" consisting of a single $(4H)^{\times}_{Si}$ adjacent to Fe^{3+} in the octahedral site, based on comparison to the most intense O-H band frequency in andradite IR spectra (Amthauer and Rossman 1998; Geiger and Rossman 2018). Furthermore, they speculated that their model for hydrogrossular clusters could be extended to assign other bands at 3581 and 3594 cm^{-1} to different sized hydroandradite clusters. This hypothesis is difficult to assess because the total Fe content in many grossular garnets is too low to accurately determine Fe^{2+}/Fe^{3+} using established methods. Our cation assignments (Table 4) based on stoichiometry using the calculation scheme of Locock (2008) indicate that all of the Fe is Fe^{2+} for our garnets with 0.06 to 1.8 wt% FeO, but this method for calculating Fe^{2+}/Fe^{3+} suffers from considerable uncertainty and Fe^{3+} may also be present.

The role of Ti in H incorporation in grossular and andradite was recently studied by Reynes et al. (2020). They proposed coupled substitution of Ti on the Y site and 2H for Si, as follows:

$$\left\{ V''''_{Si} - 2(OH)^{\cdot}_{O} \right\}^{''} + 2Ti^{\cdot\cdot}_{Al,Fe} \qquad (11)$$

FTIR spectra of the grossular studied by Reynes et al. are unusual compared to most grossular garnets surveyed by Rossman and Aines (1991), containing only three bands at 3546, 3595, and 3652 cm^{-1}; the closest match is to GRR1359, a grossular from a metarodingite in the Gruppo di Voltri, Italy (probably from a similar geologic setting as the rodingite grossular studied by

This is the peer-reviewed, final accepted version for American Mineralogist, published by the Mineralogical Society of America.
The published version is subject to change. Cite as Authors (Year) Title. American Mineralogist, in press.
DOI: https://doi.org/10.2138/am-2021-7880. http://www.minsocam.org/

687 Reynes et al.). Bands at similar frequencies are also present in spectra of the class 2b grossular
688 samples in this study, centered at 3546, 3599, and 3657 cm^{-1} in GRR1386. Therefore, this
689 mechanism may also be important in these garnets, which contain between 0.3 to 0.6 wt% TiO_2
690 (Table 4). The presence of a band at 3652-3657 cm^{-1} related to defect (11) could also partially
691 explain the imperfect correlation of F content to high frequency absorption in Figure 8a.
692 Another possibility is that some of the low frequency bands represent H substitution in
693 dodecahedral and/or octahedral sites via defects such as $(2H)^{\times}_{Ca}$ or $(3H)^{\times}_{Al}$, respectively. This
694 attribution could further help to explain the identification of two-proton clusters in GRR1386 by
695 Cho and Rossman (1993), if a large fraction of the H is located in the defects (8), (11), and
696 $(2H)^{\times}_{Ca}$ combined. Substitution of H via defects such as $(2H)^{\times}_{Ca}$ would also be consistent with
697 the higher E_a measured for lower frequency O-H bands by Reynes et al. (2018), if dehydration
698 requires counter-diffusion of Ca to take place (as opposed to dehydration via a fast-redox
699 mechanism). Although this hypothesis is highly speculative, DFT calculations for nominally
700 anhydrous minerals to date indicate that the $(4H)^{\times}_{Si}$ defect gives rise to O-H absorptions at higher
701 frequencies than substitutions involving octahedral cation vacancies. This phenomenon applies
702 to olivine (Balan et al. 2011; Umemoto et al. 2011), enstatite (Balan et al. 2013), wadsleyite
703 (Blanchard et al. 2013), and ringwoodite (Blanchard et al. 2009).
704 In principle, clumped OH-F defects in octahedral or dodecahedral sites are also possible,
705 as are coupled substitution mechanisms like those put forth by Valley et al. (1983) (Equation 5).
706 The intensity of the low-frequency bands in East African grossular also correlates positively with
707 F content (Fig. 8b). By analogy to our argument with the high frequency bands, this might
708 suggest a role for such defects in addition to clumped OH-F in tetrahedral sites. One weakness
709 with this idea is that the presence of isolated, clumped OH-F defects in octahedral or

dodecahedral sites would require the presence of Si-F bonds, because all O sites in the garnet structure are shared between the tetrahedral site, two dodecahedral sites, and the octahedral site. As noted by Smyth et al. (1990), there are no known mineral structures in which F bonds directly to tetrahedral Si. However, some NMR studies provide evidence for Si-F bonding in aluminosilicate glasses (e.g., Zeng and Stebbins 2000; Liu and Nekvasil 2002). It is probably more likely that any defect associate involving clumped OH-F in an octahedral or dodecahedral site would be paired with a neighboring defect associate in the tetrahedral site (e.g., three H and one F substituting for Si).

Coupled H and F substitution in other garnet compositions

Our model of coupled H and F substitution for Si in grossular likely applies to garnets with other compositions. Data from our 2012 session show strong correlations between ^{16}OH and ^{19}F in 11 spessartine garnets (Fig. 6b), similar to the correlations seen for East African grossular (Fig. 6a). These spessartine garnets have peaks at ~3582, 3595, 3615, 3625, 3640, and 3649 cm^{-1} (Arredondo et al. 2001). Bands at similar frequencies are also present in spectra of a spessartine with up to 3.8 wt% F studied by Smyth et al. (1990). Aines and Rossman (1984) recognized that these six peaks (which can be fit with even more bands) cannot be explained by $(4H)^{\times}_{Si}$ alone. It is tempting to assign the band at 3595 cm^{-1} (with a shoulder at 3582 cm^{-1}) to $(4H)^{\times}_{Si}$. The lower frequency compared to katoite or grossular can be explained by the high mass of Mn^{2+} (compared to Ca^{2+}) in the X-site (Geiger and Rossman 2018). However, relative peak heights at 3582 and 3595 cm^{-1} vary considerably in garnets from different parts of the pegmatite and in spessartine from the Himalayan Mine (Arredondo et al. 2001), which is not easily reconcilable with a single O-H site being responsible for both bands. Taken together, these observations

suggest the possibility that some or all of the bands represent clumped OH-F defects analogous to those we propose for grossular.

The presence of high frequency bands in some garnets along the grossular-andradite join (Phichaikamjornwut et al. 2012; Geiger and Rossman 2020a) was already noted. In the supplementary material, we provide IR spectra of a $Grs_{26}Adr_{74}$ garnet (GRR1830) and a nearly end-member andradite (GRR2103) that we analyzed by SIMS in 2012. GRR1830 has at least eight bands, with peaks at 3560, 3580, 3589, 3617, 3640, 3653, 3660, and 3677 cm^{-1}. The band locations are similar to those in the garnets from Thailand studied by Phichaikamjornwut et al. (2012). The spectrum of GRR2103 is dominated by a strong peak at 3563 cm^{-1} (with a shoulder at about 3547 cm^{-1}) and has only weak absorbance above 3600 cm^{-1}. Published spectra of other garnets close to end-member andradite also typically do not have these bands (e.g., Amthauer and Rossman 1998; Geiger and Rossman 2018). However, Amthauer and Rossman (1998) noted spectral complexity in a near-end member andradite from Stanley Butte, AZ, USA (GRR1137). Again, the number of bands in GRR1830 and the grossular-andradite garnets studied by Phichaikamjornwut et al. (2012) raises the possibility that some of them represent clumped OH-F defects. This inference is also consistent with SIMS data. Whereas GRR1830 yielded an average $^{19}F/^{18}O$ ratio of 0.191, equivalent to 76 μg/g F, measurements during the same session on GRR2103 yielded $^{19}F/^{18}O$ ratios just barely above the detection limit (<1 μg/g F; Mosenfelder and Rossman 2013a).

Coupled H-F substitution is less likely to be important in pyrope, if only because it typically contains significantly lower concentrations of both elements compared to other garnet compositions. Mosenfelder and Rossman (2012) report 0.2 to 10 μg/g F in pyrope garnets from mantle xenoliths that contain up to 135 μg/g H_2O (using the IR calibration of Bell et al. 1995).

This is the peer-reviewed, final accepted version for American Mineralogist, published by the Mineralogical Society of America.
The published version is subject to change. Cite as Authors (Year) Title. American Mineralogist, in press.
DOI: https://doi.org/10.2138/am-2021-7880. http://www.minsocam.org/

These xenoliths also contain other phases (olivine, orthopyroxene, and/or clinopyroxene) that can partition much of the available F (Mosenfelder et al. 2011; Mosenfelder and Rossman 2013a,b). Nearly end-member pyrope from the Dora Maira massif represents an unusual case; its IR spectra are unlike those of other pyrope-almandine garnets, with sharp peaks at 3602, 3641, 3651, and 3662 cm^{-1} (Rossman et al. 1989). As noted above similar bands are present in a pyrope synthesized by Geiger et al. (1991).

On the one hand, Lu and Keppler (1997) attributed the bands in Dora Maira pyrope to O-H defects associated with Li and B substitution, based on Li_2O and B_2O_3 concentrations measured by ICP-AES (inductively coupled plasma atomic emission spectroscopy). On the other hand, our attribution of high-frequency bands to clumped OH-F defects is particularly apropos in this case because some Dora Maira garnets contain inclusions of phlogopite with up to 1.6 wt% F as well as other F- and Cl-bearing phases, unequivocally indicating that they formed in a halogen-rich environment (Philippot et al. 1995). Furthermore, SIMS analyses of Dora Maira pyrope by Tenner et al. (2009) – while uncalibrated for F concentration – yielded a $^{19}F/^{30}Si$ ratio of 0.215, approximately one order of magnitude higher than ratios measured in pyrope garnets from mantle xenoliths (0.008-0.025). A rough estimate of 30 μg/g F can be derived by comparing to our SIMS data on pyrope (Mosenfelder and Rossman 2012), including MON9 from Bell et al. (1995), which was also measured by Tenner et al.

IMPLICATIONS

This work highlights technical advances in analytical methods for F and H that could facilitate future studies using garnets to constrain the activities of H_2O and F-species in fluids in equilibrium with garnet-bearing phase assemblages. The present study – including our new

This is the peer-reviewed, final accepted version for American Mineralogist, published by the Mineralogical Society of America.
The published version is subject to change. Cite as Authors (Year) Title. American Mineralogist, in press.
DOI: https://doi.org/10.2138/am-2021-7880. http://www.minsocam.org/

779 calibration for the IR molar absorption coefficient in grossular – most directly applies to geologic
780 problems in the Earth's crust. However, measurements of trace F and H in garnets from mantle
781 xenoliths may also provide additional constraints on recycling of these elements into the mantle,
782 already a topic of interest addressed by studies of F and H in olivines and pyroxenes.

783 Fine-scale zoning of H in garnets such as those from Asbestos or the garnets studied by
784 Jamtveit and Hervig (1994) or Reynes et al. (2020) is probably best studied using micro-
785 analytical techniques such as SIMS or FTIR conducted with a focal plane array (FPA) detector,
786 which is becoming more widely available (the FPA detector has a higher spatial resolution than
787 normal MCT detectors such as those we used; e.g., Reynes et al. 2020). We have also
788 demonstrated that F can be measured reliably with EPMA at levels down to ~50 μg/g, and it
789 should be possible to achieve higher analytical throughput at lower cost with EPMA compared to
790 SIMS. Furthermore, in principle, minimum estimates for F concentrations in garnet could be
791 constrained from FTIR spectra alone, once band assignments for coupled H-F defects are
792 confirmed and controversy over incorporation mechanisms is settled. We expect that theoretical
793 calculations will shed additional light on coupled H-F substitution in garnets and other nominally
794 anhydrous minerals.
795

796 **ACKNOWLEDGMENTS**

797 Financial support for this research is gratefully acknowledged from: NSF grants EAR-
798 0947956 and EAR-1322082 to George Rossman, EAR-1347908 to Jed Mosenfelder, NASA
799 80NSSC19K0959 to Marc Hirschmann, the Gordon and Betty Moore Foundation, and the
800 White Rose Foundation. The manuscript was improved by helpful reviews from Andrew Locock,
801 Jörg Hermann, and an anonymous reviewer. We also thank Yunbin Guan for assistance with

SIMS analyses and John Beckett for help operating the gas-mixing 1-atm furnace. Campbell Bridges, Peter Flusser, Robert Gaal, Peter Keller, William Larson, Gary Novak, and Julius Petsch are thanked for providing garnet samples that were used in the work.

REFERENCES

Aines, R.D., and Rossman, G.R. (1984) The hydrous component in garnets: pyralspites. American Mineralogist, 69, 116-1126.

Allen, F.M., and Buseck, P.R. (1988) XRD, FTIR, and TEM studies of optically anisotropic grossular garnets. American Mineralogist, 73, 568-584.

Amthauer, G., and Rossman, G.R. (1998) The hydrous component in andradite garnet. American Mineralogist, 83, 835–840.

Andrut, M., Wildner, M., and Beran, A. (2002) The crystal chemistry of birefringent natural uvarovites. Part IV. OH defect incorporation mechanisms in non-cubic garnets derived from polarized IR spectroscopy. European Journal of Mineralogy, 14, 1019–1026.

Armstrong, J.T. (1988) Quantitative analysis of silicate and oxide minerals, comparison of Monte Carlo, ZAF and $\phi(\rho z)$ procedures. In D.E. Newbury, Ed. Microbeam analysis, p. 239-246. San Francisco Press, San Francisco, CA.

Arredondo, E.H., Rossman, G.R., and Lumpkin, G.R. (2001) Hydrogen in spessartine-almandine garnets as a tracer of granitic pegmatite evolution. American Mineralogist, 86, 485-490.

Aubaud, C., Withers, A.C., Hirschmann, M., Guan, Y., Leshin, L.A., Mackwell, S., and Bell, D.R. (2007) Intercalibration of FTIR and SIMS for hydrogen measurements in glasses and nominally anhydrous minerals. American Mineralogist, 92, 811-828.

824 Balan, E., Refson, K., Blanchard, M., Delattre, S., Lazzeri, M., Ingrin, J., Mauri, F., Wright, K.,
825 and Winkler, B. (2008) Theoretical infrared absorption coefficient of OH groups in
826 minerals. American Mineralogist, 93, 950-953.
827 Balan, E., Ingrin, J., Delattre, S., Kovacs, I., and Blanchard, M. (2011) Theoretical infrared
828 spectrum of OH-defects in forsterite. European Journal of Mineralogy, 23, 285–292.
829 Basso, R., Giusta, A.D., and Zefiro, L. (1983) Crystal structure refinement of plazolite: a highly
830 hydrated natural hydrogrossular. Neues Jahrbuch für Mineralogie Monatshefte, H.6, 251-
831 258.
832 Basso, R., and Cabella, R. (1990) Crystal chemical study of garnets from metarodingites in the
833 Voltri Group metaophilites (Ligurian Alps, Italy). Neues Jahrbuch für Mineralogie
834 Monatshefte, H.3, 127-136.
835 Bell, D. R., and Rossman, G. R. (1992) The distribution of hydroxyl in garnets from the sub-
836 continental mantle of southern Africa. Contributions to Mineralogy and Petrology, 111,
837 161-178.
838 Bell, D.R., Ihinger, P.D., and Rossman, G.R. (1995) Quantitative analysis of trace OH in garnet
839 and pyroxene. American Mineralogist, 80, 465–474.
840 Beran, A., and Libowitzky, E. (2006) Water in natural mantle minerals II: olivine, garnet, and
841 accessory minerals. In H. Keppler and J. R. Smyth, Eds., Water in Nominally Anhydrous
842 Minerals, 62, p. 169-191. Reviews in Mineralogy and Geochemistry, Mineralogical
843 Society of America, Chantilly, Virginia.
844 Bernini, D., Wiedenbeck, M., Dolejs, D., and Keppler, H. (2012) Partitioning of halogens
845 between mantle minerals and aqueous fluids: implications for the fluid flow regime in
846 subduction zones. Contributions to Mineralogy and Petrology, 165, 117-128.

847 Berry, A., O'Neill, H.St.C., Hermann, J., and Scott, D.R. (2007) The infrared signature of water
848 associated with trivalent cations in olivine. Earth and Planetary Science Letters, 261,
849 134–142.
850 Bertie, J.E., and Lan, Z. (1996) Infrared intensities of liquids XX: the intensity of the OH
851 stretching band of liquid water revisited, and the best current values of the optical
852 constants of H_2O(I) at 25 °C between 15,000 and 1 cm^{-1}. Applied Spectroscopy 50, 1047-
853 1057. □□□□□□□□□
854 Beyer, C., Klemme, S., Wiedenbeck, M., Stracke, A., and Vollmer, C. (2012) Fluorine in
855 nominally fluorine-free mantle minerals: Experimental partitioning of F between olivine,
856 orthopyroxene and silicate melts with implications for magmatic processes. Earth and
857 Planetary Science Letters, 337-338, 1-9.
858 Birkett, T.C., and Trzcienski, W.E. (1984) Hydrogarnet: multi-site hydrogen occupancy in the
859 garnet structure. Canadian Mineralogist, 22, 675-680.
860 Blanchard, M., Balan, E., and Wright, K. (2009) Incorporation of water in iron-free ringwoodite:
861 a first-principles study. American Mineralogist, 94, 83–89.
862 Blanchard, M., Roberge, M., Balan, E., Fiquet, G., and Bureau, H. (2013) Infrared signatures of
863 OH defects in wadsleyite: A first-principles study. American Mineralogist, 98, 2132–
864 2143.
865 Blanchard M., Ingrin J., Balan E., Kovács I., and Withers A.C. (2017) Effect of iron and trivalent
866 cations on OH defects in olivine. American Mineralogist, 102, 302-311.
867 Burdo, R.A., and Morrison, G.H. (1971) Table of atomic and molecular lines for spark source
868 mass spectrometry of complex sample-graphite mixes. Report no. 1670. Materials
869 Science Center, Cornell University, Ithaca, New York.

Bureau, H., Raepsaet, C., Khodja, H., Carraro, A., and Aubaud, C. (2009) Determination of hydrogen content in geological samples using elastic recoil detection analysis (ERDA). Geochimica et Cosmochimica Acta 73, 3311–3322.

Burns, R.G., and Strens R.G.J. (1966) Infrared study of the hydroxyl bands in clinoamphiboles. Science, 153, 890-892

Chakhmouradian, A.R., Cooper, M.A., Medici, L., Hawthorne, F.C., and Adar, F. (2008) Fluorine-rich hibschite from silicocarbonatite, Afrikanda complex, Russia: crystal chemistry and conditions of crystallization. Canadian Mineralogist, 46, 1033-1042.

Chantler, C.T., Olsen, K., Dragoset, R.A., Chang, J., Kishore, A.R., Kotochigova, S.A., and Zucker, D.S. (2005) X-Ray Form Factor, Attenuation and Scattering Tables (version 2.1). [Online] Available: http://physics.nist.gov/ffast. National Institute of Standards and Technology, Gaithersburg, MD.

Cho, H., and Rossman, G.R. (1993) Single-crystal NMR studies of low-concentration hydrous species in minerals: grossular garnet. American Mineralogist, 78, 1149-1164.

Cohen-Addad, C., Ducros, P., and Bertaut, E.F. (1967) Étude de la substitution du groupement SiO_4 par (OH)4 dans les composés $Al_2Ca_3(OH)_{12}$ et $Al_2Ca_3(SiO4)_{2.16}(OH)_{3.36}$ de type grenat. Acta Crystallographica, 23, 220–230.

Crépisson, C., Blanchard, M., Bureau, H., Sanloup, C., Withers, A.C., Khodja, H., Surble, S., Raepsaet, C., Beneut, K., Leroy, C., Giura, P., and Balan, E. (2014) Clumped fluoride-hydroxyl defects in forsterite: implications for the upper-mantle. Earth and Planetary Science Letters, 390, 287–295.

Dalou, C., Koga, K.T., Shimizu, N., Boulon, J., and Devidal, J.L. (2012) Experimental determination of F and Cl partitioning between lherzolite and basaltic melt. Contributions to Mineralogy and Petrology, 163, 591-609.

Donovan, J.J., Lowers, H.A., and Rusk, B.G. (2011) Improved electron probe microanalysis of trace elements in quartz. American Mineralogist, 96, 274-282.

Fitzsimons, I.C.W., Harte, B., and Clark, R.M. (2000) SIMS stable isotope measurement: counting statistics and analytical precision. Mineralogical Magazine, 64, 59–83.

Flohr, M.J.K., and Ross, M. (1989) Alkaline igneous rocks of Magnet Cove, Arkansas: metasomatized ijolite xenoliths from Diamond Jo quarry. American Mineralogist, 74, 113-131.

Geiger, C.A., and Armbruster, T. (1997) $Mn_3Al_2Si_3O_{12}$ spessartine and $Ca_3Al_2Si_3O_{12}$ grossular garnet: dynamical structural and thermodynamic properties. American Mineralogist, 82, 740–747.

Geiger, C.A., and Rossman, G.R. (1994) Crystal field stabilization energies of almandine-pyrope and almandine-spessartine garnets determined by FTIR near infrared measurements. Physics and Chemistry of Minerals, 21, 516-525.

Geiger, C.A., and Rossman, G.R. (2018) IR spectroscopy and OH- in silicate garnet: the long quest to document the hydrogarnet substitution. American Mineralogist, 103, 384-393.

Geiger, C.A., and Rossman, G.R. (2020a) Micro- and nano-size hydrogarnet clusters and proton ordering in calcium silicate garnet: Part I. The quest to understand the nature of “water” in garnet continues. American Mineralogist, 105, 455-467.

912 Geiger, C.A., and Rossman, G.R. (2020b) Micro- and nano-size hydrogarnet clusters in calcium
913 silicate garnet: Part II. Mineralogical, petrological, and geochemical aspects. American
914 Mineralogist, 105, 468-478.
915 Geiger, C.A., Langer, K., Bell, D.R., Rossman, G.R., and Winkler, B. (1991) The hydroxide
916 component in synthetic pyrope. American Mineralogist, 76, 49–59.
917 Geiger, C.A., Stahl, A., and Rossman, G.R. (2000) Single-crystal IR- and UV/ VIS-spectroscopic
918 measurements on transition-metal-bearing pyrope: The incorporation of hydroxide in
919 garnet. European Journal of Mineralogy, 12, 259–271.
920 Giuliani, G., Ohnenstetter, D., Palhol, F., Feneyrol, J., Boutroy, E., de Boissezon, H., and
921 Lhomme, T. (2008) Karelianite and vanadian phlogopite from the Merelani Hills gem
922 zoisite deposits, Tanzania. Canadian Mineralogist, 46, 1183-1194.
923 Giuliani, G., Fallick, A.E., Feneyrol, J., Ohnenstetter, D., Pardieu, V., and Saul, M. (2011)
924 $^{18}O/^{16}O$ and V/Cr ratios in gem tsavorites from the Neoproterozoic Mozambique
925 metamorphic belt: a clue towards their origins? Mineralium Deposita, 46, 671-676.
926 Grew, E., Locock, A.J., Mills, S.J., Galuskina, I.O., Galuskin, E.V., and Hålenius, U. (2013)
927 Nomenclature of the garnet supergroup. American Mineralogist, 98, 785-811.
928 Grützner, T., Kohn, S.C. Bromiley, D.W., Rohrbach, A., Berndt, J., and Klemme, S. (2017) The
929 storage capacity of fluorine in olivine and pyroxene under upper mantle conditions.
930 Geochimica et Cosmochimica Acta, 208, 160–170.
931 Guggino, S.N., and Hervig, R.L. (2011) Synthesis and characterization of five new F-bearing
932 basalt reference materials (Fba glasses): quantifying the fluorine content of the basaltic
933 glass standards BCR-2G, BHVO-2G, GSA-1G, GSC-1G, GSD-1G, GSE-1G, ML3B-G,

KL2-G, and ALV-519-4. American Geophysical Union, Fall Meeting 2011, abstract #V31C-2535.

Harmon, K.M., Gabriele, J.M., and Nuttal, A.S. (1982) Hydrogen bonding in the tetrahedral $O_4H_4^{4-}$ cluster in hydrogrossular. Journal of Molecular Structure, 82, 213–219.

Hauri, E.H., Wang, J., Dixon, J.E.,, King, P.L., Mandeville, C., and Newman, S. (2002) SIMS analysis of volatiles in silicate glasses 1. Calibration, matrix effects and comparisons with FTIR. Chemical Geology, 183, 99-114.

Hervig, R.L., and Bell, D.R. (2005) Fluorine and hydrogen in mantle megacrysts. American Geophysical Union, Fall Meeting 2005, abstract V41A-1426.

Ingrin, J., and Blanchard, M. (2006) Diffusion of hydrogen in minerals. In H. Keppler and J.R. Smyth, Eds., Water in Nominally Anhydrous Minerals, 62, p. 291–320, Reviews in Mineralogy and Geochemistry, Mineralogical Society of America, Chantilly, Virginia.

Jamtveit, B., and Hervig, R.L. (1994) Constraints on transport and kinetics in hydrothermal systems from zoned garnet crystals. Science, 263, 505-508.

Johnson E. A., and Rossman G. R. (2003) The concentration and speciation of hydrogen in feldspars using FTIR and ^{1}H MAS NMR spectroscopy. American Mineralogist, 88, 901–911.

Johnson E. A., and Rossman G. R. (2004) A survey of hydrous species and concentrations in igneous feldspars. American Mineralogist, 89, 586–600.

Kalinichenko, A.M, Proshko, Y.Ya, Matyash, LV., Pavlishin, V.L, and Gamarnik, M.Ya. (1987) Geochemistry international, 24, 132-135.

955 Khomenko, V.M., Langer, K., Beran, A., Koch-Mu¨ ller, M., and Fehr, T. (1994) Titanium
956 substitution and OH-bearing defects in hydrothermally grown pyrope crystals. Physics
957 and Chemistry of Minerals, 20, 483-488.
958 Klemme, S., and Stalder, R. (2018) Halogens in the Earth's mantle: what we know and what we
959 don't. In D.E. Harlov and L. Aranovich, Eds., The Role of Halogens in Terrestrial and
960 Extraterrestrial Geochemical Processes, p. 847-869. Springer, Cham, Switzerland.
961 Koga, K., Hauri, E., Hirschmann, M.M., and Bell, D. (2003) Hydrogen concentration analyses
962 using SIMS and FTIR: comparison and calibration for nominally anhydrous minerals.
963 Geochemistry, Geophysics, and Geosystems, 4, doi: 10.1029/2002GC000378.
964 Kröger, F., and Vink, H. (1956) Relations between the concentrations of imperfections in
965 crystalline solids. In F. Seitz and D. Turnbull, Eds., Solid state physics, 3. Elsevier,
966 Amsterdam, pp. 307-435.
967 Kurka, A., Blanchard, M., and Ingrin, J. (2005) Kinetics of hydrogen extraction and deuteration
968 in grossular. Mineralogical Magazine, 69, 359–371.
969 Lager, G.A., Armbruster, T., and Faber, G. (1987) Neutron and X-ray diffraction study of
970 hydrogarnet Ca3Al2(O4H4)3. American Mineralogist, 72, 756–765.
971 Lager, G.A., Armbruster, T., Rotella, F.J., and Rossman G.R. (1989) OH substitution in garnets:
972 X-ray and neutron diffraction, infrared, and geometric-modeling studies. American
973 Mineralogist 74, 840–851.
974 Libowitzky, E., and Beran, A. (1995) OH defects in forsterite. Physics and Chemistry of
975 Minerals, 22, 387–392.
976 Libowitzky, E., and Rossman, G.R. (1997) An IR absorption calibration for water in minerals.
977 American Mineralogist, 82, 1111-1115.

978 Liu, Y., and Nekvasil, H. (2002) Si-F bonding in aluminosilicate glasses: Inferences from ab
979 initio NMR calculations. American Mineralogist, 87, 339-346.
980 Locock, A.J. (2008) An excel spreadsheet to recast analyses of garnet into end-member
981 components, and a synopsis of the crystal chemistry of natural silicate garnets.
982 Computers and Geosciences, 34, 1769-1780.
983 Lu, R., and Keppler, H. (1997) Water solubility in pyrope to 100 kbar. Contributions to
984 Mineralogy and Petrology, 129, 35-42.
985 Maldener, J., Hösch, A., Langer, K., and Rauch, F. (2003) Hydrogen in some natural garnets
986 studied by nuclear reaction analysis and vibrational spectroscopy. Physics and Chemistry
987 of Minerals, 30, 337-344.
988 Manning, C.E., and Bird, D.K. (1990) Fluorian garnets from the host rocks of the Skaergaard
989 intrusion: implications for metamorphic fluid composition. American Mineralogist, 75,
990 859-873.
991 Mosenfelder, J.L., and Rossman, G.R. (2012) Fluorine in the mantle: the role of nominally
992 anhydrous minerals. American Geophysical Union, Fall Meeting 2012, Abstract FDI54A-
993 06.
994 Mosenfelder, J.L., and Rossman, G.R. (2013a) Analysis of hydrogen and fluorine in pyroxenes: I.
995 Orthopyroxene. American Mineralogist, 98, 1026-1041.
996 Mosenfelder, J.L., and Rossman, G.R. (2013b) Analysis of hydrogen and fluorine in pyroxenes:
997 part II. Clinopyroxene. American Mineralogist, 98, 1042-1054.
998 Mosenfelder, J.L., Le Voyer, M., Rossman, G.R., Guan, Y., Bell, D.R., Asimow, P.D., and Eiler,
999 J.M. (2011) Analysis of hydrogen in olivine by SIMS: evaluation of standards and
1000 protocol. American Mineralogist, 96, 1725-1741.

1001 Mosenfelder, J.L., Rossman, G.R., and Johnson, E.A. (2015) Hydrous species in feldspars: a
1002 reassessment based on FTIR and SIMS. American Mineralogist, 100, 1209-1221.
1003 Mosenfelder, J.L., Andrys, J.L., von der Handt, A., Kohlstedt, D.L., and Hirschmann, M.M.
1004 (2020) Hydrogen incorporation in plagioclase. Geochimica et Cosmochimica Acta, 277,
1005 87–110.
1006 O'Leary, J.A., Rossman, G.R., and Eiler, J.M. (2007) Hydrogen analysis in minerals by
1007 continous-flow mass spectrometry. American Mineralogist, 92, 1990-1997.
1008 Paterson, M.S. (1982) The determination of hydroxyl by infrared absorption in quartz, silicate
1009 glasses, and similar materials. Bulletin de Minéralogie, 105, 20-29.
1010 Phichaikamjornwut, B., Skogby, H., Ounchanum, P., Limtrakun, P., and Boonsoong, A. (2012)
1011 Hydrous components of grossular-andradite garnets from Thailand: thermal stability and
1012 exchange kinetics. European Journal of Mineralogy, 24, 107-121.
1013 Philippot, P., Chevallier, P., Chopin, C., and Dubessy, J. (1995) Fluid composition and evolution
1014 in coesite-bearing rocks (Dora-Maira massif, Western Alps): implications for element
1015 recycling during subduction. Contributions to Mineralogy and Petrology, 121, 29-44.
1016 Raepsaet, C., Bureau, H., Khodja, H., Aubaud, C., and Carraro, A. (2008) μ-ERDA
1017 developments in order to improve the water content determination in hydrous and
1018 nominally anhydrous mantle phases. Nuclear Instruments and Methods in Physics
1019 Research Section B: Beam Interactions with Materials and Atoms 266, 1333–1337.
1020 Reynes, J., Jollands, M., Hermann, J., and Ireland, T. (2018) Experimental constraints on
1021 hydrogen diffusion in garnet. Contributions to Mineralogy and Petrology, 173, 69.

1022 Reynes, J., Lanari, P., and Hermann, J. (2020) A mapping approach for the investigation of Ti–
1023 OH relationships in metamorphic garnet. Contributions to Mineralogy and Petrology, 175,
1024 46.
1025 Roberge, M., Bureau, H., Bolfan-Casanova, N., Frost, D.J., Raepsaet, C., Surble, S., Khodja, H.,
1026 Auzende, A.-L., Fiquet, G. (2015) Is the transition zone a deep reservoir for fluorine?
1027 Earth and Planetary Science Letters, 429, 25-32.
1028 Rossman, G.R. (2006) Analytical methods for measuring water in nominally anhydrous minerals.
1029 In H. Keppler and J. R. Smyth, Eds., Water in Nominally Anhydrous Minerals, 62, p. 1-
1030 28. Reviews in Mineralogy and Geochemistry, Mineralogical Society of America,
1031 Chantilly, Virginia.
1032 Rossman, G.R., and Aines, R.D. (1986) Spectroscopy of birefringent grossular from Asbestos,
1033 Quebec, Canada. American Mineralogist, 71, 779-780.
1034 Rossman, G.R., and Aines, R.D. (1991) The hydrous components in garnets: grossular-
1035 hydrogrossular. American Mineralogist, 76, 1153-1164.
1036 Rossman, G.R., Beran, A., and Langer, K. (1989) The hydrous component of pyrope from the
1037 Dora Maira Massif, Western Alps. European Journal of Mineralogy, 1, 151–154.
1038 Schingaro, E., Lacalamita, M., Mesto, E., Ventruti, G., Pedrazzi, G., Ottolini, L., and Scordari., F.
1039 (2016) Crystal chemistry and light elements analysis of Ti-rich garnets. American
1040 Mineralogist, 101, 371-384.
1041 Slack, G.A., and Chrenko, R.M. (1971) Optical absorption of natural garnets from 1000 to 30000
1042 wavenumbers. Journal of the Optical Society of America, 61, 1325-1329.

1043 Smyth, J.R., Madel, R.E., McCormick, T.C., Munoz, J.L., and Rossman, G.R. (1990) Crystal-
1044 structure refinement of a F-bearing spessartine garnet. American Mineralogist, 75, 314-
1045 318.
1046 Sykes, D., Rossman, G., Veblen, D., and Grew, E. (1994) Enhanced H and F incorporation in
1047 borian olivine. American Mineralogist, 79, 904–908.
1048 Tenner, T.J., Hirschmann, M.M., Withers, A.C., and Hervig, R.L. (2009) Hydrogen partitioning
1049 between nominally anhydrous upper mantle minerals and melt between 3 and 5 GPa.
1050 Chemical Geology, 262, 42–56.
1051 Umemoto K., Wentzcovitch R.M., Hirschmann M.M., Kohlstedt D.L., and Withers A.C. (2011)
1052 A first-principles investigation of hydrous defects and IR frequencies in forsterite: the
1053 case for Si vacancies. American Mineralogist. 96, 1475-1479.
1054 Valley, J.W., Essene, E.J., and Peacor, D.R. (1983) Fluorine-bearing garnets in Adirondack calc-
1055 silicates. American Mineralogist, 68, 444-448.
1056 Verma, R.K. (1960) Elasticity of some high-density crystals. Journal of Geophysical Research 65,
1057 757-766.
1058 Vermeesch, P. (2018) IsoplotR: A free and open toolbox for geochronology. Geoscience
1059 Frontiers, 9, 1479-1493.
1060 Visser, D. (1993) Fluorine-bearing hydrogarnets from Blengsvatn, Bamble sector, South Norway.
1061 Mineralogy and Petrology, 47, 209-218.
1062 White, W.B., and Moore, R.K. (1972) Interpretation of the spin allowed bands of Fe^{2+} in silicate
1063 garnets. American Mineralogist, 57, 1692-1710.
1064 Withers, A.C., and Behrens, H. (1999) Temperature-induced changes in the NIR spectra of

hydrous albitic and rhyolitic glasses between 300 and 100 K. Physics and Chemistry of Minerals, 27, 119-132.

Withers, A.C., Wood, B.J., and Carroll, M.R. (1998) The OH content of pyrope at high pressure. Chemical Geology, 147, 161-171.

Withers, A.C., Bureau, H., Raepsaet, C., and Hirschmann, M.M. (2012) Calibration of infrared spectroscopy by elastic recoil detection analysis of H in synthetic olivine. Chemical Geology, 334, 92-98.

Witter, J.B., and Kuehner, S.M. (2004) A simple empirical method for high-quality electron microprobe analysis of fluorine at trace levels in Fe-bearing minerals and glasses. American Mineralogist, 89, 57-63.

York, D., Evensen, N.M., Martínez, M.L., and De Basebe Delgado, J. (2004) Unified equations for the slope, intercept, and standard errors of the best straight line. American Journal of Physics, 72, 367-375.

Yoshino, T. and Vazhakuttiyakam, J. (2018) Fluorine solubility in bridgmanite: A potential fluorine reservoir in the Earth's mantle. Earth and Planetary Science Letters, 504, 106-114.

Zeng, Q., and Stebbins, J.F. (2000) Flourine sites in aluminosilicate glasses: High resolution ^{19}F NMR results. American Mineralogist, 85, 863–867.

Zhang, C., Koepke, J., Wang, L-X., Wolff, P.E., Wilke, S., Stechern, A., Almeev, R., and Holtz, F. (2016) A practical method for accurate measurement of trace level fluorine in Mg- and Fe-Bearing minerals and glasses using electron probe microanalysis. Geostandards and Analytical Research, doi: 10.1111/j.1751-908X.2015.00390.x.

TABLES

Table 1. Garnet sample localities and FTIR data

Table 2. Results of elastic recoil detection analysis compared to other H calibration techniques

Table 3. SIMS data

Table 4. EPMA data and calculated garnet end members

FIGURE CAPTIONS

FIGURE 1. Representative FTIR spectra for grossular spectral classes 2, 2b, 3, 4, and 7. Class designations follow Rossman and Aines (1991). Spectra are plotted without baseline correction and offset from each other for clarity. Spectra in **a** and **b** are normalized to 1 cm; spectra in **c** are normalized to different thicknesses (as labeled) to facilitate comparison. (**a)** Class 2 (GRR42), with the strongest peak at 3647 cm^{-1}, and class 2b (GRR1386). Class 2b has peaks below 3620 cm^{-1} that are almost absent in GRR42. Room temperature spectrum of GRR1386 (solid black curve) is directly overlain by spectrum taken at 77 K (grey dashed curve). (**b)** Class 2b (GRR732) and class 7 (GRR1122). Although these spectra have bands at similar positions, in class 7 the dominant peaks are at lower frequencies and the strongest peak is at 3599 cm^{-1} rather than 3647 cm^{-1}. (**c)** Class 3 and 4 spectra of natural and synthetic grossular garnets. Three representative spectra of JLM83a are displayed, with integrated absorbances (Abs_{tot}) equal to 691 (dotted line), 1118 (dashed line), and 1526 cm^{-2} (solid line). The spectrum of GRR53 is from the slice labeled "GRR53B-F" displayed in Figure 6 of Rossman and Aines (1991). Spectra of synthetic, end-member grossular crystals are from Geiger and Armbruster (1997) and Withers et al. (1998). Spectral classes 3 and 4 are nominally distinguished by whether the strongest peak is at 3631 or 3621 cm^{-1}, respectively. Three of these garnets (GRR53, JLM83a, and the grossular

made by Geiger and Armbruster) have strong peaks at 3689, 3677, 3665, and/or 3559 cm^{-1} that are weak or absent in the other two samples (GRR1537 and the grossular synthesized by Withers et al.).

FIGURE 2. Detailed comparison near the baselines of 77 K and 298 K spectra of GRR1386. The band at ~3240 cm^{-1} at 77 K is attributed to frozen H_2O in fluid inclusions. Bands attributed to structural OH^- groups are off scale. Spectra of liquid water from Bertie and Lan (1996) and ice from Johnson and Rossman (2003) also plotted for comparison. GRR1386 spectra are normalized to 1 cm thickness; spectra of ice and water are arbitrarily scaled.

FIGURE 3. Raw (uncorrected) H_2O concentrations determined by ERDA for three East African grossular garnets (GRR732, GRR771, and GRR1756) and blank forsterite (GRR1017), as a function of integrated absorbance (Abs_{tot}). Solid line is a York regression. Dashed lines represent 95% confidence intervals calculated from *a priori* errors. Equation and mean squared weighted deviation (MSWD) of the fit are also shown.

FIGURE 4. $^{16}OH/^{18}O$ data from two SIMS sessions. Error bars not shown are within the symbol size. Solid lines are York regressions fit to data (circles) on the blank and East African samples only, with 95% confidence intervals (calculated from *a priori* errors) displayed as dashed curves. The equation and MSWD for each regression are also displayed in the graphs. **(a)** 2012 data. Each point represents the average of three to five measurements, with $2s_x$ (sample standard deviation) error bars displayed for $^{16}OH/^{18}O$. **(b)** 2016 data. In this plot, each point represents a

single analysis. Consequently, uncertainties in $^{16}OH/^{18}O$ ($2s_{\bar{x}}$, standard error of the mean) are all within the symbol size in this plot. Some data points are obscured by overlap with other data; all original data are given in the supplementary material.

FIGURE 5. Backscattered electron image of JLM83a after SIMS analysis. H_2O and F concentrations (in μg/g) are displayed above (up and to the left) each SIMS crater (black spot). Analysis numbers in order of collection are labeled to the lower right of each spot. The analyses with asterisks (analyses 15-18) were compromised by elevated background $^{16}OH^-$ and $^{19}F^-$, as discussed in the text. Cycle profiles (uncalibrated depth profiles) for analyses 12 and 20 are displayed in supplementary Figure S8.

FIGURE 6. Correlations between ^{16}OH and ^{19}F for grossular and spessartine. (**a)** SIMS data for grossular from sessions in 2012 (open symbols) and 2016 (closed symbols). Each symbol represents a single analysis ($2s_{\bar{x}}$ uncertainties are within the symbol size for each point). Solid lines are ordinary least-squares (OLS) regressions to data for East African grossular garnets (r^2 = 0.98) and multiple analyses on Asbestos grossular JLM83a (r^2= 0.99). Data on JLM83a that were compromised by contamination (Fig. 5) are not included in this plot. (**b)** Spessartine data from 2012 session. Each data point on this plot represents an average of between four and 11 analyses for one sample ($2s_x$ uncertainties are within the symbol size). Solid line is an OLS regression (r^2 = 0.99) to all of the data.

FIGURE 7. Comparison of ERDA results (circles) to previous calibration data on Asbestos grossular (GRR53 and GRR53B, triangles; Aines and Rossman 1984; Rossman and Aines 1991), Maldener et al. (2003, diamonds), and O'Leary et al. (2007, square). Only two data points from the compilation of Rossman and Aines (1991) are plotted (for Asbestos garnets GRR53 and GRR53F), but the original regression determined for their entire data set of grossular and hydrogrossular garnets over a much wider range of H contents (up to 12.75 wt% H_2O) is displayed as a dashed line. The ERDA data have been blank corrected in this graph by subtracting 100 μg/g from the raw values plotted in Figure 3.

FIGURE 8. Results of spectral curve fitting plotted as function of calculated F (per formula unit). Frequencies of fitted bands vary by up to 3 cm^{-1}. Symbols (see inset legend in **a**) correspond to those in Figure 7. (**a)** Integrated absorbance *vs.* F for fitted bands centered at ~3631, 3643, 3647, 3657, 3664, 3674, and 3688 cm^{-1}. (**b)** Integrated absorbance vs. F for fitted bands centered at ~3530, 3539, 3545, 3560, 3567, 3582, 3600, 3608, and 3622 cm^{-1}.

FIGURES

This is the peer-reviewed, final accepted version for American Mineralogist, published by the Mineralogical Society of America.
The published version is subject to change. Cite as Authors (Year) Title. American Mineralogist, in press.
DOI: https://doi.org/10.2138/am-2021-7880. http://www.minsocam.org/

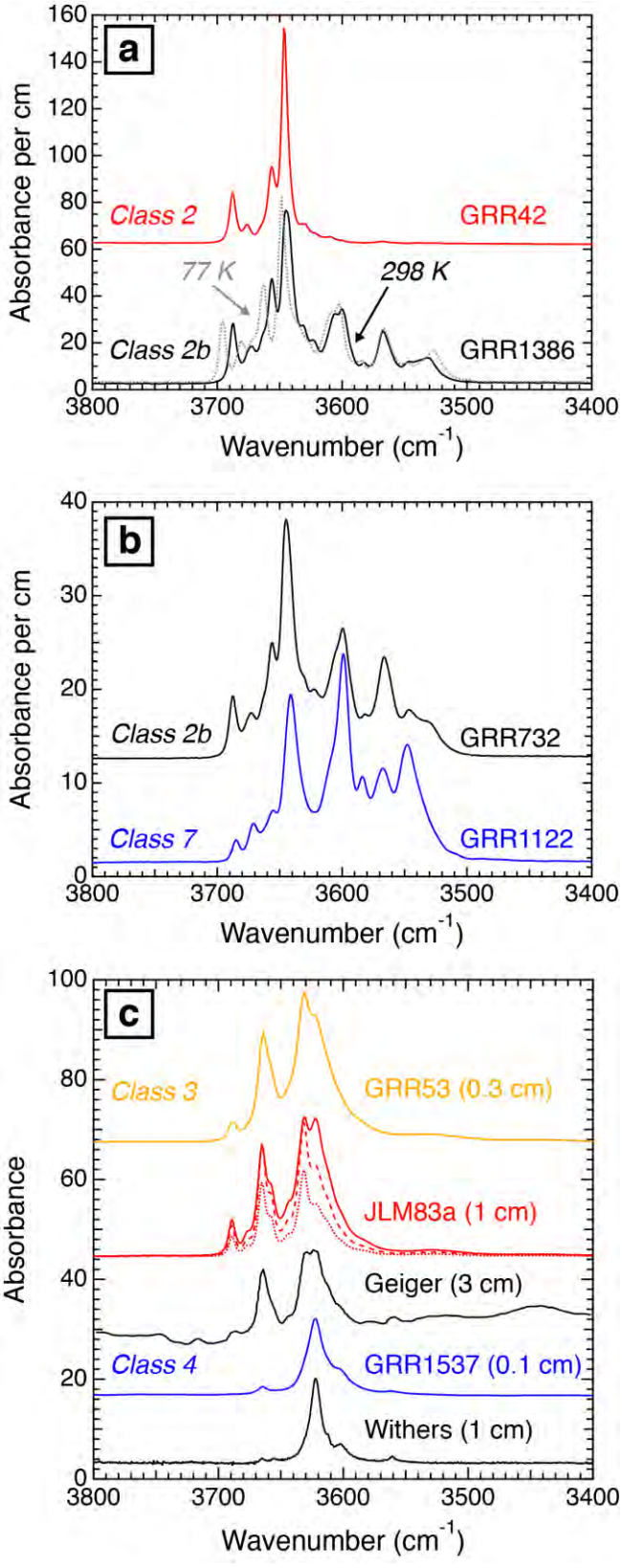

1181

FIGURE 1. Representative FTIR spectra for grossular spectral classes 2, 2b, 3, 4, and 7. Class designations follow Rossman and Aines (1991). Spectra are plotted without baseline correction and offset from each other for clarity. Spectra in **a** and **b** are normalized to 1 cm; spectra in **c** are normalized to different thicknesses (as labeled) to facilitate comparison. (**a)** Class 2 (GRR42), with the strongest peak at 3647 cm^{-1}, and class 2b (GRR1386). Class 2b has peaks below 3620 cm^{-1} that are almost absent in GRR42. Room temperature spectrum of GRR1386 (solid black curve) is directly overlain by spectrum taken at 77 K (grey dashed curve). (**b)** Class 2b (GRR732) and class 7 (GRR1122). Although these spectra have bands at similar positions, in class 7 the dominant peaks are at lower frequencies and the strongest peak is at 3599 cm^{-1} rather than 3647 cm^{-1}. (**c)** Class 3 and 4 spectra of natural and synthetic grossular garnets. Three representative spectra of JLM83a are displayed, with integrated absorbances (Abs_{tot}) equal to 691 (dotted line), 1118 (dashed line), and 1526 cm^{-2} (solid line). The spectrum of GRR53 is from the slice labeled "GRR53B-F" displayed in Figure 6 of Rossman and Aines (1991). Spectra of synthetic, end-member grossular crystals are from Geiger and Armbruster (1997) and Withers et al. (1998). Spectral classes 3 and 4 are nominally distinguished by whether the strongest peak is at 3631 or 3621 cm^{-1}, respectively. Three of these garnets (GRR53, JLM83a, and the grossular made by Geiger and Armbruster) have strong peaks at 3689, 3677, 3665, and/or 3559 cm^{-1} that are weak or absent in the other two samples (GRR1537 and the grossular synthesized by Withers et al.).

1205

1206

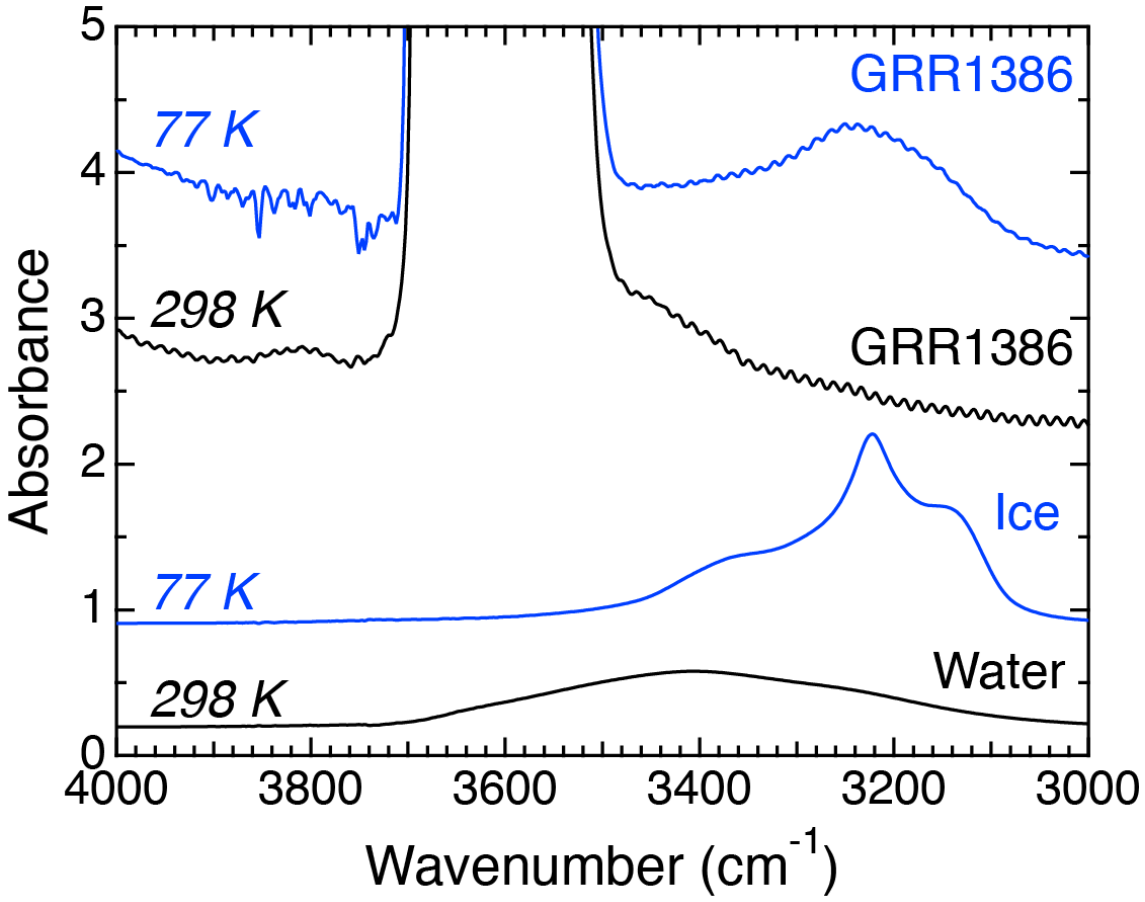

1207

1208 **FIGURE 2.** Detailed comparison near the baselines of 77 K and 298 K spectra of GRR1386.

1209 The band at ~3240 cm^{-1} at 77 K is attributed to frozen H_2O in fluid inclusions. Bands attributed

1210 to structural OH^- groups are off scale. Spectra of liquid water from Bertie and Lan (1996) and ice

1211 from Johnson and Rossman (2003) also plotted for comparison. GRR1386 spectra are

1212 normalized to 1 cm thickness; spectra of ice and water are arbitrarily scaled.

1213

This is the peer-reviewed, final accepted version for American Mineralogist, published by the Mineralogical Society of America.
The published version is subject to change. Cite as Authors (Year) Title. American Mineralogist, in press.
DOI: https://doi.org/10.2138/am-2021-7880. http://www.minsocam.org/

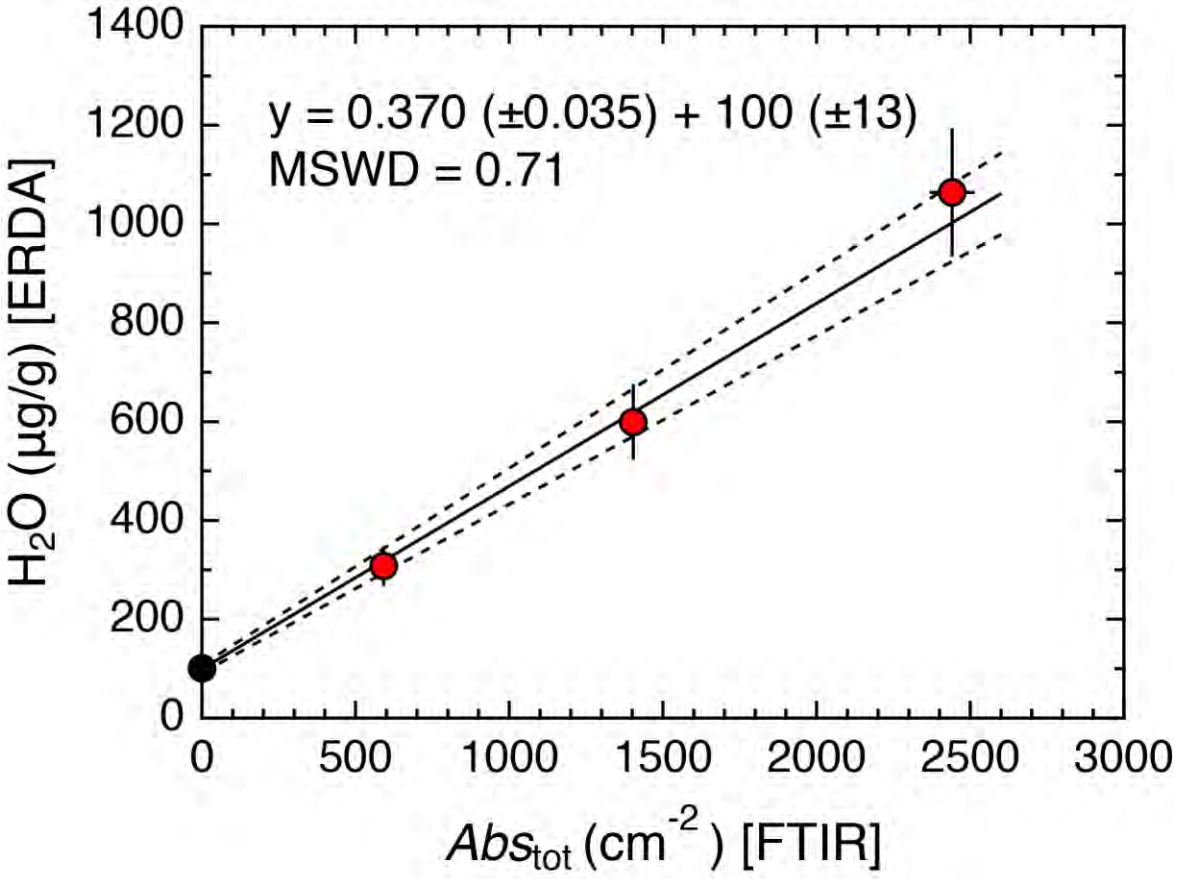

FIGURE 3. Raw (uncorrected) H_2O concentrations determined by ERDA for three East African grossular garnets (GRR732, GRR771, and GRR1756) and blank forsterite (GRR1017), as a function of integrated absorbance (Abs_{tot}). Solid line is a York regression. Dashed lines represent 95% confidence intervals calculated from *a priori* errors. Equation and mean squared weighted deviation (MSWD) of the fit are also shown.

This is the peer-reviewed, final accepted version for American Mineralogist, published by the Mineralogical Society of America.
The published version is subject to change. Cite as Authors (Year) Title. American Mineralogist, in press.
DOI: https://doi.org/10.2138/am-2021-7880. http://www.minsocam.org/

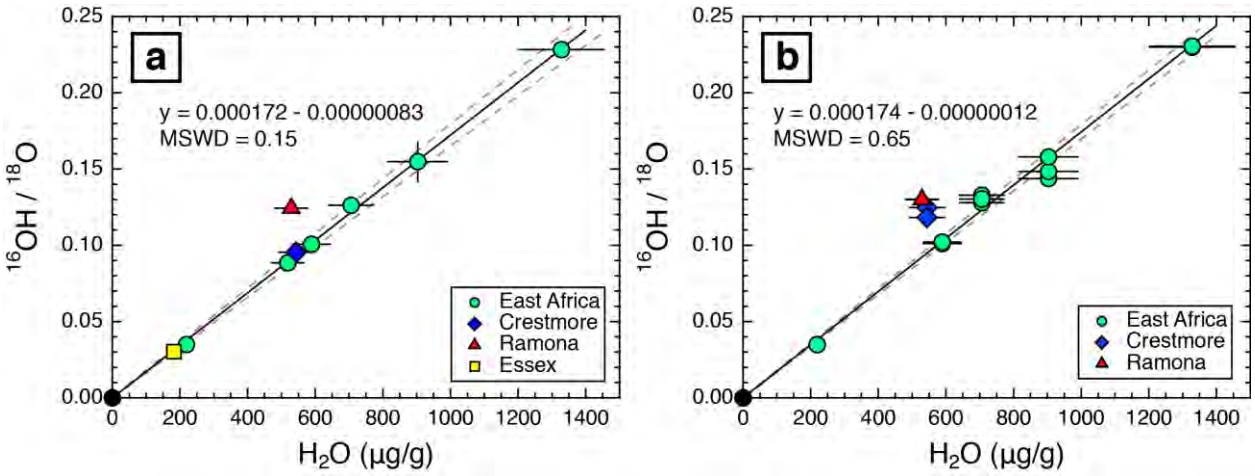

FIGURE 4. $^{16}OH/^{18}O$ data from two SIMS sessions. Error bars not shown are within the symbol size. Solid lines are York regressions fit to data (circles) on the blank and East African samples only, with 95% confidence intervals (calculated from *a priori* errors) displayed as dashed curves. The equation and MSWD for each regression are also displayed in the graphs. **(a)** 2012 data. Each point represents the average of three to five measurements, with $2s_x$ (sample standard deviation) error bars displayed for $^{16}OH/^{18}O$. **(b)** 2016 data. In this plot, each point represents a single analysis. Consequently, uncertainties in $^{16}OH/^{18}O$ ($2s_{\bar{x}}$, standard error of the mean) are all within the symbol size in this plot. Some data points are obscured by overlap with other data; all original data are given in the supplementary material.

This is the peer-reviewed, final accepted version for American Mineralogist, published by the Mineralogical Society of America.
The published version is subject to change. Cite as Authors (Year) Title. American Mineralogist, in press.
DOI: https://doi.org/10.2138/am-2021-7880. http://www.minsocam.org/

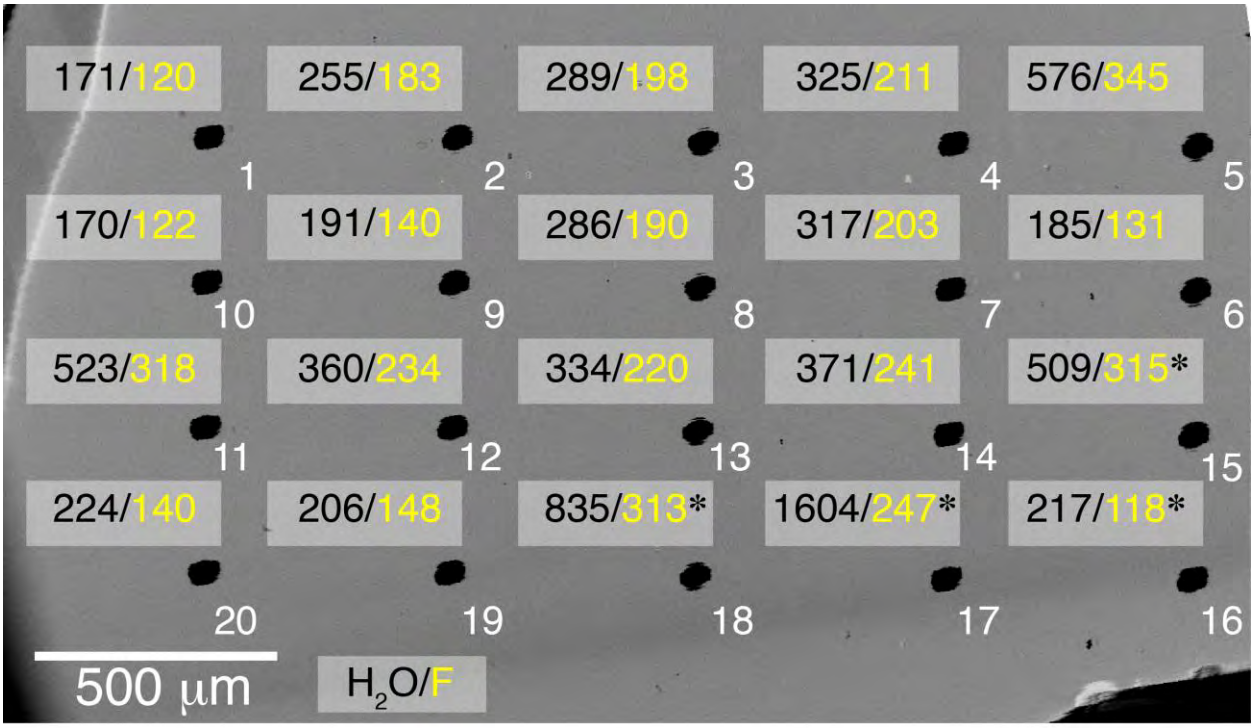

FIGURE 5. Backscattered electron image of JLM83a after SIMS analysis. H_2O and F concentrations (in μg/g) are displayed above (up and to the left) each SIMS crater (black spot). Analysis numbers in order of collection are labeled to the lower right of each spot. The analyses with asterisks (analyses 15-18) were compromised by elevated background $^{16}OH^-$ and $^{19}F^-$, as discussed in the text. Cycle profiles (uncalibrated depth profiles) for analyses 12 and 20 are displayed in supplementary Figure S8.

This is the peer-reviewed, final accepted version for American Mineralogist, published by the Mineralogical Society of America.
The published version is subject to change. Cite as Authors (Year) Title. American Mineralogist, in press.
DOI: https://doi.org/10.2138/am-2021-7880. http://www.minsocam.org/

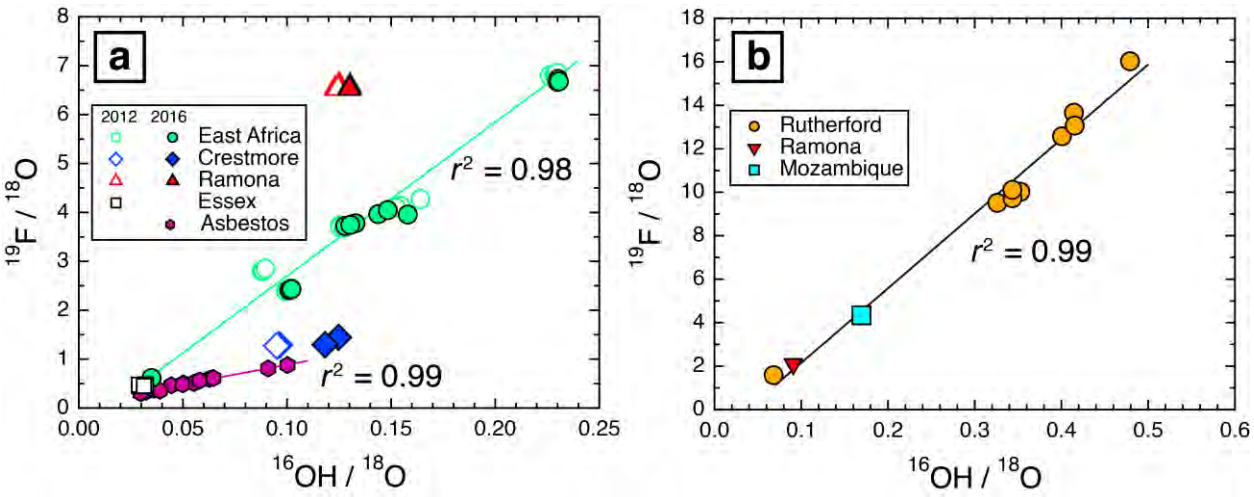

FIGURE 6. Correlations between ^{16}OH and ^{19}F for grossular and spessartine. (**a)** SIMS data for grossular from sessions in 2012 (open symbols) and 2016 (closed symbols). Each symbol represents a single analysis ($2s_{\bar{x}}$ uncertainties are within the symbol size for each point). Solid lines are ordinary least-squares (OLS) regressions to data for East African grossular garnets (r^2 = 0.98) and multiple analyses on Asbestos grossular JLM83a (r^2= 0.99). Data on JLM83a that were compromised by contamination (Fig. 5) are not included in this plot. (**b)** Spessartine data from 2012 session. Each data point on this plot represents an average of between four and 11 analyses for one sample ($2s_x$ uncertainties are within the symbol size). Solid line is an OLS regression (r^2 = 0.99) to all of the data.

This is the peer-reviewed, final accepted version for American Mineralogist, published by the Mineralogical Society of America.
The published version is subject to change. Cite as Authors (Year) Title. American Mineralogist, in press.
DOI: https://doi.org/10.2138/am-2021-7880. http://www.minsocam.org/

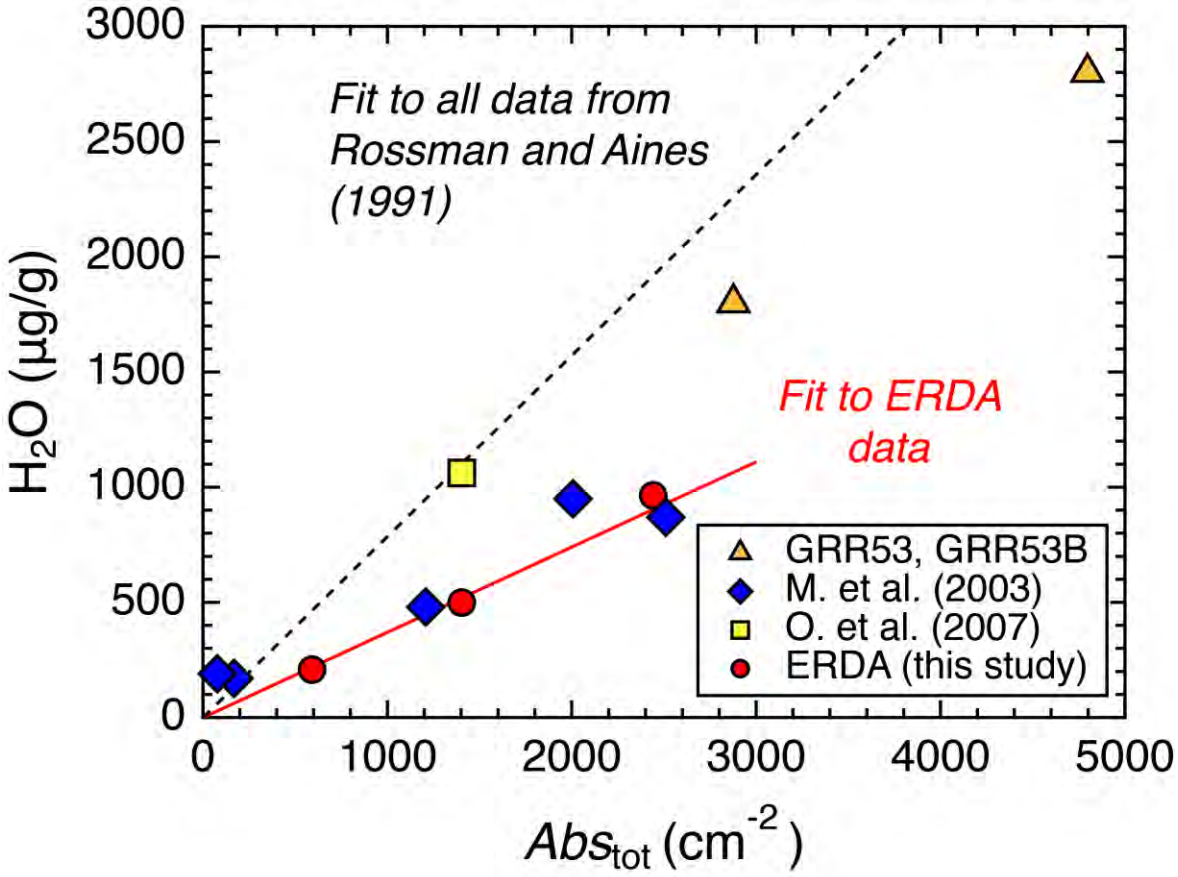

FIGURE 7. Comparison of ERDA results (circles) to previous calibration data on Asbestos grossular (GRR53 and GRR53B, triangles; Aines and Rossman 1984; Rossman and Aines 1991), Maldener et al. (2003, diamonds), and O'Leary et al. (2007, square). Only two data points from the compilation of Rossman and Aines (1991) are plotted (for Asbestos garnets GRR53 and GRR53F), but the original regression determined for their entire data set of grossular and hydrogrossular garnets over a much wider range of H contents (up to 12.75 wt% H_2O) is displayed as a dashed line. The ERDA data have been blank corrected in this graph by subtracting 100 µg/g from the raw values plotted in Figure 3.

This is the peer-reviewed, final accepted version for American Mineralogist, published by the Mineralogical Society of America.
The published version is subject to change. Cite as Authors (Year) Title. American Mineralogist, in press.
DOI: https://doi.org/10.2138/am-2021-7880. http://www.minsocam.org/

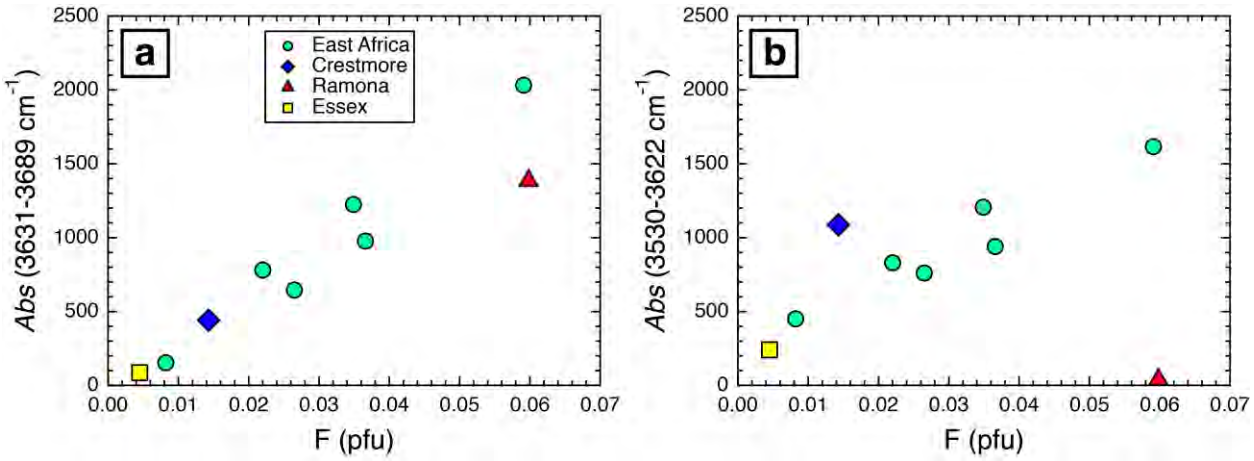

FIGURE 8. Results of spectral curve fitting plotted as function of calculated F (per formula unit). Frequencies of fitted bands vary by up to 3 cm^{-1}. Symbols (see inset legend in **a**) correspond to those in Figure 7. (**a)** Integrated absorbance *vs.* F for fitted bands centered at ~3631, 3643, 3647, 3657, 3664, 3674, and 3688 cm^{-1}. (**b)** Integrated absorbance vs. F for fitted bands centered at ~3530, 3539, 3545, 3560, 3567, 3582, 3600, 3608, and 3622 cm^{-1}.

This is the peer-reviewed, final accepted version for American Mineralogist, published by the Mineralogical Society of America.
The published version is subject to change. Cite as Authors (Year) Title. American Mineralogist, in press.
DOI: https://doi.org/10.2138/am-2021-7880. http://www.minsocam.org/

Table 1: Garnet sample localities and FTIR data

Sample No.	Locality	Spectral class[a]	Abs_{tot} (cm^{-2})	Mean wavenumber (cm^{-1})
GRR42	Ramona Mine, California, U.S.A.	2	1430(14)	3647
GRR229	Stream gravel, Merelani Hills, Tanzania	2b	1909(38)	3623
GRR732	Mindi Hills, Kenya	2b	1403(28)	3617
GRR771	Merelani Hills, Tanzania	2b	2441(73)	3622
GRR1122	Crestmore Mine, California, U.S.A.	7	1471(44)	3597
GRR1386	Stream gravel, Merelani Hills, Tanzania	2b	3589(72)	3633
GRR1386a	Stream gravel, Merelani Hills, Tanzania	2b	1592(48)	3619
GRR1429	Essex Country, New York, U.S.A.	7	493(38)	3570-3579[b]
GRR1756	#2 reef, Scorpion Mine, Voi, Taita, Kenya	7	591(12)	3595
JLM83a	Asbestos, Quebec, Canada	3	691-1544[c]	3630-3631[c]

Notes: uncertainties in parentheses are estimated as discussed in text.

[a] Classification scheme of Rossman and Aines (1991)

[b] Range of values for 7 spectra

[c] Range measured in 48 spectra

This is the peer-reviewed, final accepted version for American Mineralogist, published by the Mineralogical Society of America.
The published version is subject to change. Cite as Authors (Year) Title. American Mineralogist, in press.
DOI: https://doi.org/10.2138/am-2021-7880. http://www.minsocam.org/

Table 2: Results of elastic recoil detection analysis (ERDA) compared to other H calibration techniques

Sample No.	Phase	Abs_{tot} (cm^{-2})	H_2O, μg/g		Reference	Method
			Uncorrected	Blank corrected		
GRR1756	Grossular	591(12)	308(40)	208(40)	This study	ERDA
GRR732	Grossular	1403(28)	599(76)	499(76)	This study	ERDA
			–	1062(31)	1	CFMS
GRR771	Grossular	2441(73)	1064(130)	964(130)	This study	ERDA
NSL1	Rhyolitic glass		11,133(1399)	11,033 (1399)	This study	ERDA
			–	11,600	2	KFT-FTIR
N3	Rhyolitic glass		33,658 (4209)	33,558 (4209)	This study	ERDA
			–	33,000	2	KFT-FTIR
N5	Rhyolitic glass		50,549 (6313)	50,449 (6313)	This study	ERDA
			–	50,600	2	KFT-FTIR
GRR1017 [a]	Forsterite	0	101(14)	0	This study	ERDA
GRR53	Grossular	2877	–	1800	3, 4	MEA, MAN
GRR53F	Grossular	4796	–	2800	4	^{19}F NRA
HESS1	Grossular	2510	–	870	5	^{15}N NRA
		2006	–	950	5	^{15}N NRA
TSAV	Grossular	1208	–	480	5	^{15}N NRA
MALI	Grossular	168	–	170	5	^{15}N NRA
GRMALI	Grossular	77	–	190	5	^{15}N NRA

Notes: References: 1 = O'Leary et al. (2007); 2= Tenner et al. (2009); 3 = Aines and Rossman (1984); 4 = Rossman and A
CFMS = continuous-flow mass spectrometry; KFT-FTIR = Karl-Fischer titration and FTIR; MEA = P_2O_5 coulometry (mo
Uncertainties in parentheses are 2*s* in terms of least units cited

[a]Blank reference material used to correct ERDA data.

ıines (1991); 5 = Maldener et al. (2003)

›isture evolution analyzer); MAN = evolved H_2 gas volume (manometry); NRA = nuclear reaction analysis

This is the peer-reviewed, final accepted version for American Mineralogist, published by the Mineralogical Society of America.
The published version is subject to change. Cite as Authors (Year) Title. American Mineralogist, in press.
DOI: https://doi.org/10.2138/am-2021-7880. http://www.minsocam.org/

Table 3: SIMS data

Sample no.	SIMS session	No. of analyses	H_2O, μg/g [a]	$^{16}O^{1}H/^{18}O$
GRR1122-HT	2012	4	0	0.000338 – 0.000450 [c]
	2016	3	0	0.001365 – 0.001904 [c]
GRR42	2012	5	529(50)	0.1244(14)
	2016	2[d]		0.1300, 0.1302
GRR229	2012	4	706(68)	0.1262(16)
	2016	3		0.1304(49)
GRR732	2012	4	519(50)	0.0885(16)
GRR771	2012	4	903(90)	0.155(13)
	2016	3		0.150(15)
GRR1122	2012	4	544(54)	0.0956(12)
	2016	2[d]		0.1183, 0.1247
GRR1386	2012	4	1328(128)	0.2283(31)
	2016	3		0.2302(6)
GRR1386a	2012	4	589(58)	0.1007(23)
	2016	3		0.1016(10)
GRR1429	2012	4	182(22)	0.0303(34)
GRR1756	2012	4	219(21)	0.0349(2)
	2016	2[d]		0.349, 0.349[d]
JLM83a[e]	2016	16[f]	256-571	0.0296–0.1002

Notes: Numbers in parentheses are 2*s* uncertainties in terms of least units cited.

[a] Values calculated from FTIR using calibration factor of 0.37 (Eq. 1), with uncertainties propag

[b] Values calculated from $^{16}O^{1}H/^{18}O$ using working curve for F-bearing glasses.

[c] Uncorrected ratios, given as a range.

[d] For samples with only two analyses, each analysis is given (separated by comma).

[e]Values for this sample are given as a range (for both FTIR and SIMS analyses).

[f] Four analyses were rejected owing to a spike in the blank, as described in the text.

$^{19}F/^{18}O$	F, µg/g [b]
1.279(21)	508 (8)
1.325(40)	537(84)
6.563(69)	2606(27)
6.529, 6.584	2559, 2581
3.713(48)	1474(19)
3.751(57)	1470(22)
2.819(49)	1119(19)
4.14(19)	1644(75)
3.99(10)	1565(39)
1.281(16)	508(6)
1.295, 1.447	508, 567
6.824(49)	2709(19)
6.694(64)	2624(25)
2.422(48)	962(19)
2.423(16)	950(6)
0.465(34)	185(13)
0.602(4)	239(2)
0.611, 0.615[d]	239, 241
0.3502–0.8789	120–345

gated as described in text.

This is the peer-reviewed, final accepted version for American Mineralogist, published by the Mineralogical Society of America.
The published version is subject to change. Cite as Authors (Year) Title. American Mineralogist, in press.
DOI: https://doi.org/10.2138/am-2021-7880. http://www.minsocam.org/

Table 4: EPMA data and calculated garnet end members

Sample No.	GRR42	GRR229	GRR732	GRR771	GRR1122
SiO_2	38.59(24)	38.77(24)	40.15(39)	39.84(18)	38.69(31)
TiO_2	–	0.40(3)	0.34(3)	0.54(2)	0.57(6)
Al_2O_3	21.43(12)	20.94(13)	21.97(28)	22.34(8)	17.64(7)
Cr_2O_3	–	0.28(2)	0.04(3)	–	–
V_2O_3	–	1.90(3)	0.88(1)	0.05(2)	–
FeO[a]	3.23(2)	0.08(1)	0.06(3)	0.14(2)	7.53(26)
MnO	0.10(2)	0.90(5)	1.15(1)	0.27(3)	0.38(4)
MgO	–	0.47(2)	0.54(3)	0.34(1)	0.07(2)
CaO	35.33(6)	35.10(14)	35.44(33)	36.25(10)	34.61(20)
H_2O^+	0.0723[b]	0.0706[c]	0.0519[c]	0.0903[c]	0.0544[c]
F	0.2477(36)	0.1516(30)	0.1119[e]	0.1470(62)	0.0586(62)
O=F	-0.1	-0.06	-0.05	-0.06	-0.02
Total	98.90	99.00	100.68	99.95	99.58
Recalculated					
FeO	1.16	0.08	0.06	0.14	2.09
Fe_2O_3	2.30	–	–	–	6.05
Recalculated Total[f]	99.13	99.00	100.68	99.95	100.19
Si	2.9457	2.9576	3.0015	2.9906	2.9804
Ti	–	0.0230	0.0191	0.0305	0.0330
Al^{VI}	1.8978	1.8583	1.9357	1.9764	1.5924
Al^{IV}	0.0301	0.0243	–	–	0.0091
Cr	–	0.0169	0.0024	–	–
V	–	0.1162	0.0527	0.0030	–
Fe^{2+}	0.0738	0.0051	0.0038	0.0088	0.1346
Fe^{3+}	0.1324	–	–	–	0.3506
Mn	0.0065	0.0582	0.0728	0.0172	0.0248
Mg	–	0.0534	0.0602	0.0380	0.0080
Ca	2.8896	2.8689	2.8387	2.9155	2.8566
H_4	0.0092	0.0090	0.0065	0.0113	0.0070
O	11.9402	11.9699	12.0027	11.9959	11.9857
F	0.0598	0.0366	0.0265	0.0349	0.0143
End Members					
Katoite	0.31%	0.30%	0.22%	0.38%	0.23%
FCa garnet	0.50%	0.30%	0.22%	0.29%	0.12%

Schorlomite-Al	–	1.15%	–	–	0.45%
Morimotoite	–	–	–	–	2.40%
Majorite	–	–	–	–	–
Goldmanite	–	5.81%	2.64%	0.15%	–
Uvarovite	–	0.84%	0.12%	–	–
Spessartine	0.22%	1.94%	2.43%	0.57%	0.83%
Pyrope	–	1.78%	2.01%	1.27%	0.27%
Almandine	2.46%	0.17%	0.13%	0.29%	3.69%
Grossular	91.41%	87.22%	91.43%	96.02%	74.49%
Andradite	4.11%	–	–	–	17.53%
Remainder	1.00%	0.48%	0.82%	1.03%	0.00%
Total	100.01%	99.99%	100.02%	100.00%	100.01%

Notes: Cation assignments and garnet end members calculated using Locock (2008), on an 8

See Locock (2008) for definition of end members. "Remainder" represents the proportion of ca
Dashed lines denote oxides, elements or end members below detection limit or calculated to b
EPMA data represent averages (in wt%, with 1s uncertainties in parentheses) of 5 to 6 analys

[a] Total Fe calculated as FeO.

[b] H_2O calculated from 2012 SIMS data, using fit to data for East African grossulars.

[c] H_2O calculated from FTIR data (Table 3).

[d] H_2O and F based on 2016 SIMS data, for two analyses at extreme ends of range.

[e] F based on 2012 SIMS data.

[f] Recalculated wt% total after calculation of Fe^{2+}/Fe^{3+}.

GRR1386	GRR1386a	GRR1429	GRR1756	JLM83a	
				low	*high*
39.19(23)	39.96(5)	39.48(16)	39.70(11)	39.95(18)	39.95(18)
0.64(3)	0.36(3)	0.42(3)	0.40(1)	–	–
22.29(7)	21.90(5)	18.62(13)	20.90(12)	22.23(13)	22.23(13)
–	–	–	0.29(2)	–	–
–	–	–	1.77(5)	–	–
0.20(3)	1.36(5)	7.27(9)	0.06(1)	1.82(10)	1.82(10)
0.14(2)	0.33(2)	0.21(2)	0.97(1)	0.24(3)	0.24(3)
0.43(1)	0.31(1)	0.14(1)	0.57(1)	–	–
36.27(11)	35.78(6)	34.11(9)	35.02(5)	35.51(14)	35.51(14)
0.1328[c]	0.0589[c]	0.0182[c]	0.0219[c]	0.0171[d]	0.0576[d]
0.2478(24)	0.0924(29)	0.0185[e]	0.0343(42)	0.012[d]	0.0345[d]
-0.10	-0.04	-0.01	-0.01	-0.01	-0.01
99.44	100.11	100.28	99.73	99.77	99.83
0.2	1.36	3.48	0.06	1.82	1.82
–	–	4.22	–	–	–
99.44	100.11	100.71	99.73	99.77	99.83
2.9536	3.0037	3.0137	3.0079	3.0162	3.0138
0.0363	0.0204	0.0241	0.0228	–	–
1.9650	1.9401	1.6752	1.8663	1.9781	1.9765
0.0149	–	–	–	–	–
–	–	–	0.0174	–	–
–	–	–	0.1075	–	–
0.0126	0.0855	0.2219	0.0038	0.1149	0.1148
–	–	0.2422	–	–	–
0.0089	0.0210	0.0136	0.0622	0.0153	0.0153
0.0483	0.0310	0.0022	0.0644	–	–
2.9289	2.8817	2.7899	2.8429	2.8726	2.8703
0.0167	0.0074	0.0023	0.0028	0.0022	0.0072
11.9523	11.9850	11.9955	12.0229	12.0053	12.0031
0.0591	0.0220	0.0045	0.0082	0.0029	0.0082
0.56%	0.25%	0.08%	0.09%	0.07%	0.24%
0.49%	0.18%	0.04%	0.07%	0.02%	0.07%

This is the peer-reviewed, final accepted version for American Mineralogist, published by the Mineralogical Society of America.
The published version is subject to change. Cite as Authors (Year) Title. American Mineralogist, in press.
DOI: https://doi.org/10.2138/am-2021-7880. http://www.minsocam.org/

0.75%	–	–	–	–	–
–	2.04%	2.41%	–	–	–
–	0.37%	0.07%	–	–	–
–	–	–	5.38%	–	–
–	–	–	0.87%	–	–
0.30%	0.70%	0.45%	2.07%	0.51%	0.51%
1.61%	0.66%	–	2.15%	–	–
0.42%	1.78%	6.36%	0.13%	3.64%	3.50%
94.87%	93.43%	76.83%	88.36%	94.66%	94.50%
–	–	12.11%	–	–	–
1.00%	0.59%	1.65%	0.89%	1.10%	1.18%
100.00%	100.00%	100.00%	100.01%	100.00%	100.00%

cation basis (treating H as H_4^{4+}).

ations that could not be allocated.

be 0.

es for all samples except JLM83a (average of 36 analyses).